Thermosphere extension of the Whole Atmosphere Community Climate Model

H.-L. Liu,[1] B. T. Foster,[1] M. E. Hagan,[1] J. M. McInerney,[1] A. Maute,[1] L. Qian,[1] A. D. Richmond,[1] R. G. Roble,[1] S. C. Solomon,[1] R. R. Garcia,[2] D. Kinnison,[2] D. R. Marsh,[2] A. K. Smith,[2] J. Richter,[3] F. Sassi,[4] and J. Oberheide[5]

Received 20 April 2010; revised 5 August 2010; accepted 3 September 2010; published 4 December 2010.

[1] In atmospheric and space environment studies it is key to understand and to quantify the coupling of atmospheric regions and the solar impacts on the whole atmosphere system. There is thus a need for a numerical model that encompasses the whole atmosphere and can self-consistently simulate the dynamic, physical, chemical, radiative, and electrodynamic processes that are important for the Sun-Earth system. This is the goal for developing the National Center for Atmospheric Research (NCAR) Whole Atmosphere Community Climate Model (WACCM). In this work, we report the development and preliminary validation of the thermospheric extension of WACCM (WACCM-X), which extends from the Earth's surface to the upper thermosphere. The WACCM-X uses the finite volume dynamical core from the NCAR Community Atmosphere Model and includes an interactive chemistry module resolving most known neutral chemistry and major ion chemistry in the middle and upper atmosphere, and photolysis and photoionization. Upper atmosphere processes, such as nonlocal thermodynamic equilibrium, radiative transfer, auroral processes, ion drag, and molecular diffusion of major and minor species, have been included in the model. We evaluate the model performance by examining the quantities essential for the climate and weather of the upper atmosphere: the mean compositional, thermal, and wind structures from the troposphere to the upper thermosphere and their variability on interannual, seasonal, and daily scales. These quantities are compared with observational and previous model results.

Citation: Liu, H.-L., et al. (2010), Thermosphere extension of the Whole Atmosphere Community Climate Model, *J. Geophys. Res.*, *115*, A12302, doi:10.1029/2010JA015586.

1. Introduction

[2] The Earth's upper atmosphere, including the mesosphere, thermosphere, and ionosphere, constitutes about 0.1% of the total air mass and is the region where solar X-ray, EUV and most UV radiation are absorbed and energetic particles are deposited. The upper atmosphere has been shown to be sensitive to the varying solar and magnetospheric inputs, and can vary significantly on time scales ranging from minutes to a solar cycle. To understand and forecast such variability is a major goal of space weather research. The Earth's upper atmosphere is also closely connected to atmospheric processes below. A classical problem is the anomalous summer-to-winter temperature gradient in the mesosphere and mesopause region. This anomalous temperature structure coincides with the reversal of the zonal wind at middle and high latitudes. The reversal is believed to be caused by adiabatic cooling and warming associated with the mean meridional circulation driven by gravity wave breaking. Most gravity waves are excited by tropospheric processes. As their amplitudes grow exponentially with altitude, they will cause larger variability before they become unstable and break [e.g., *Fritts and Alexander*, 2003, and references therein]. Gravity wave forcing is also the likely cause of the semiannual oscillation (SAO) of the mesospheric zonal wind at low latitudes [*Dunkerton*, 1982; *Garcia et al.*, 1997]. The turbulent mixing from gravity wave breaking in the mesosphere and lower thermosphere (MLT) plays an important role in the exchange of constituents between the mesosphere and thermosphere, which may in turn control the thermospheric density [*Qian et al.*, 2009]. The high-speed components of the gravity waves can penetrate into the thermosphere and ionosphere. These waves can cause traveling ionospheric disturbances (TIDs) [*Hines*, 1960], and are candidates for seeding the sporadic E

[1]High Altitude Observatory, National Center for Atmospheric Research, Boulder, Colorado, USA.
[2]Atmospheric Chemistry Division, National Center for Atmospheric Research, Boulder, Colorado, USA.
[3]Climate and Global Dynamics, National Center for Atmospheric Research, Boulder, Colorado, USA.
[4]Space Science Division, Naval Research Laboratory, Washington, D. C., USA.
[5]Department of Physics and Astronomy, Clemson University, Clemson, South Carolina, USA.

0148-0227/10/2010JA015586

and spread F layers [e.g., *Fejer and Kelley*, 1980]. The waves reaching the thermosphere are dissipated by the increasing molecular viscosity, which will lead to divergence of the wave flux of momentum and the secondary generation of gravity waves that can propagate further into the upper thermosphere [*Vadas and Fritts*, 2001]. The propagation of the secondary waves is influenced by the thermosphere temperature and wind (and thus the solar activity) [*Vadas and Fritts*, 2006], and can cause large thermospheric and ionospheric variability [*Vadas and Liu*, 2009].

[3] Atmospheric tides and planetary waves are excited by lower atmospheric processes, such as latent heat release, IR heating through water vapor, wind interaction with topography, and instability [e.g., *Forbes*, 1995]. Additionally, atmospheric thermal tides are also excited in the stratosphere due to solar UV absorption by ozone. Atmospheric tides and the planetary waves with the largest scales can propagate into the middle and upper atmosphere [*Charney and Drazin*, 1961]. As these waves propagate upward, their amplitudes grow exponentially as the density decreases, introducing large variability in the MLT. The climatology of the tides and planetary waves in the MLT has been quantified from satellite and ground based observations [e.g., *Hays and Wu*, 1994; *Burrage et al.*, 1995b; *McLandress et al.*, 1996; *Chang and Avery*, 1997; *Yu et al.*, 1997; *Vincent et al.*, 1998; *Ward et al.*, 1999; *Oberheide and Gusev*, 2002; *She*, 2004; *Oberheide et al.*, 2006; *Forbes et al.*, 2008; *Wu et al.*, 2008a, 2008b; *Xu et al.*, 2009], as well as modeling studies [e.g., *Forbes*, 1995; *Hagan et al.*, 1995, 1999; *McLandress*, 2002a, 2002b; *Ward et al.*, 2005]. Observations have also revealed that the atmospheric tides can undergo strong short-term variability [e.g., *Nakamura et al.*, 1997; *Pancheva*, 2000; *Pancheva and Mitchell*, 2004; *She et al.*, 2004]. Causes of the short-term tidal variability are also likely tied to the lower atmosphere: variability of wave sources and nonlinear interaction of tides and planetary waves [*Hagan et al.*, 1997; *Forbes et al.*, 1999; *Hagan and Roble*, 2001; *Mayr et al.*, 2003; *Lieberman et al.*, 2004; *Liu et al.*, 2007; *Chang et al.*, 2009]. Tides also display large variability over semiannual, annual, and interannual scales [*Burrage et al.*, 1995a; *McLandress*, 2002a, 2002b; *Wu et al.*, 2008a, 2008b; *Xu et al.*, 2009], and the cause of such oscillations is still an active research topic.

[4] The large-scale waves may also interact with the mean flow. For example, rapid increase of quasi-stationary planetary wave amplitudes has been regarded as the cause of stratospheric sudden warming (SSW) [*Matsuno*, 1971]. These planetary waves can propagate up to the winter mesopause, so that large mesosphere changes may precede the peak stratospheric warming [*Liu and Roble*, 2005; *Manney et al.*, 2009]. During the SSW, the large stratospheric wind change alters the gravity waves that propagate into the upper atmosphere, which in turn leads to changes in the MLT [*Myrabø et al.*, 1984; *Walterscheid et al.*, 2000; *Liu and Roble*, 2002; *Coy et al.*, 2005; *Ren et al.*, 2008]. Planetary waves and SSW are also tied to the tropospheric climate system and the stratospheric state, such as the El Niño–Southern Oscillation (ENSO) and quasi-biennial oscillation (QBO) [e.g., *Sassi et al.*, 2004; *Manzini et al.*, 2006; *Holton and Tan*, 1980]. *Sassi et al.* [2004] demonstrated using WACCM the teleconnection pattern of a warmer stratosphere, cooler mesosphere and warmer lower thermosphere at high latitudes in the winter hemisphere and warmer polar mesosphere in the summer hemisphere during ENSO periods. *Becker and Fritts* [2006] showed that the cross-hemispheric propagation of planetary waves is a major cause of the MLT temperature change in the summer hemisphere during SSW. Such variation may be related to variations in the occurrence of noctilucent clouds (NLC) [*Karlsson et al.*, 2009].

[5] The tides and planetary waves are known to affect the ionospheric variability through wind dynamo processes [e.g., *Richmond*, 1983; *Heelis*, 2004]. The nonmigrating diurnal eastward propagating wavenumber 3 signature in the ionosphere has been identified by the IMAGE satellite [*Sagawa et al.*, 2005; *Immel et al.*, 2006], and studied numerically by *Hagan et al.* [2009]. Persistent large ionospheric perturbations identified during SSW periods are thought to be associated with planetary waves and their interaction with tides [*Goncharenko and Zhang*, 2008; *Chau et al.*, 2009; *Liu et al.*, 2010].

[6] Upper atmospheric variability is also linked to the lower atmosphere through constituent transport. For example, the increasing greenhouse gases in the troposphere can be transported into the middle and upper atmosphere. *Roble and Dickinson* [1989] demonstrated that an increase of the CO_2 leads to significant radiative cooling of the thermosphere, and *Qian et al.* [2006] used the measured tropospheric CO_2 mixing ratio over the last three decades to specify the CO_2 lower boundary condition in the upper atmosphere Global Mean Model, and found that the density trend from the model is consistent with that derived from satellite drag over the corresponding period of time. The occurrence of NLCs at lower latitudes in recent years is also conjectured to be related to the increase of water vapor in the mesosphere and/or a cooling trend in the mesosphere, in response to tropospheric climate change [*Thomas*, 1996]. Downward transport provides another venue for upper-lower atmosphere coupling. SABER observations have shown that the NO_x generated in the auroral zone can be transported downward into the mesosphere and even into the stratosphere in the polar winter, especially following a strong SSW [*Randall et al.*, 2009]. The detailed mechanism and the implications for stratospheric ozone and stratospheric dynamics are not well understood.

[7] To better understand and quantify these complex interactions of the lower and upper atmosphere, as well as the atmospheric impacts from the solar output and magnetosphere, there is a need for a comprehensive model that can self-consistently simulate the dynamical, physical, chemical, radiative and electrodynamic processes that are important for the Sun-Earth system. The specific needs for a ground-to-exosphere general circulation model (GCM), as outlined by *Roble* [2000], stem from studies of physical and chemical interactions, climate variability and climate change, climate response to solar variability, space weather, and interpretation of global observations. These research requirements have prompted the coupling and/or merging of models of the lower, middle and upper atmosphere. Early exploratory efforts include the development of the National Center for Atmospheric Research (NCAR) Middle Atmosphere Community Climate Model (MACCM) [*Boville*, 1995], and the coupling of the NCAR Thermosphere-Ionosphere-

Mesosphere-Electrodynamics general circulation model (TIME-GCM) with the Community Climate Model (CCM) [*Roble*, 2000, and references therein]. These efforts further underline the need for a whole atmosphere model, and thus motivate the development of the NCAR Whole Atmosphere Community Climate Model (WACCM), as well as several other whole atmosphere models, including the Canadian Middle Atmosphere Model (CMAM), Hamburg Model of the Neutral and Ionized Atmosphere (HAMMONIA), Navy Operational Global Atmospheric Prediction System Advanced Level Physics High Altitude (NOGAPS-ALPHA), Whole Atmosphere Model (WAM) and Kyushu GCM [*Beagley et al.*, 1997; *Schmidt et al.*, 2006; *McCormack et al.*, 2004; *Akmaev et al.*, 2008; *Miyoshi and Fujiwara*, 2003]. WACCM development started around the year 2000, and the model has already been widely used by the community for studying atmospheric dynamics, chemistry, climate and coupling (a list of WACCM related publications can be found at http://waccm.acd.ucar.edu/Pubs/index.shtml). The current standard WACCM includes interactive neutral and ion chemistry and extends to the lower thermosphere. In this study, we report the extension of the WACCM (WACCM-X) to the upper thermosphere, with the inclusion of thermospheric physics adapted from the NCAR TIME-GCM [*Roble and Ridley*, 1994], and validation of the model results with observations and previous model results. The validation focuses on the aspects of fundamental importance for the upper atmospheric climate and weather: the mean structures of composition, temperature and wind, and their variability on interannual, seasonal, and daily scales.

[8] An overview of the major model components of WACCM and a description of the new model components of WACCM-X are given in section 2, followed by a presentation of compositional structures, temperature and wind structures, longitudinal structures and tides, and short-term variability in the upper atmosphere obtained from the model in section 3. A summary is given in section 4.

2. Model Components

[9] The thermosphere extension of the Whole Atmosphere Community Climate Model (WACCM-X) is based on the NCAR Whole Atmosphere Community Climate Model (WACCM), which in turn is a superset of the NCAR Community Atmospheric Model (CAM). The current version of CAM used here is version 3 (CAM3 and WACCM3). A detailed description of the WACCM3 is given by *Garcia et al.* [2007].

[10] WACCM-X uses the same finite volume dynamical core as in WACCM3 and CAM3 [*Lin*, 2004], and includes all the physics and chemistry modules in WACCM3 and CAM3. The chemistry module is interactive with the dynamics through transport and exothermic heating, and is derived from the three-dimensional (3-D) chemical transport Model for Ozone and Related chemical Tracers (MOZART) [*Brasseur et al.*, 1998; *Hauglustaine et al.*, 1998; *Horowitz et al.*, 2003; *Kinnison et al.*, 2007]. Photolysis rates at wavelengths between Lyman-α and 350nm are calculated according to *Woods and Rottman* [2002], and following *Froehlich* [2000] for wavelengths longer than 350nm. For wavelengths shortward of Lyman-α (extreme ultraviolet, or EUV and X-ray), both photolysis and photoionization are calculated following *Solomon and Qian* [2005]. The production and loss of electrons and 5 ions (O^+, O_2^+, NO^+, N^+, and N_2^+), as well as the neutral species of interests to the thermosphere and ionosphere, are calculated by the model. It should be noted, however, that the transport of the ions and electrons due to drift in electric and magnetic field or ambipolar diffusion is not included in the current model.

[11] For radiative heating, the calculation in WACCM-X is the same as that in WACCM3. WACCM3 combines the standard longwave (LW) formulation used in CAM3 and the LW nonlocal thermodynamic equilibrium (NLTE) parameterization for the 15 μm band of CO_2 and 5.3 μm band of NO [*Fomichev et al.*, 1998; *Kockarts*, 1980], which are required for the mesosphere and lower thermosphere (MLT) region. For shortwave (SW) radiation, WACCM3 merged the CAM3 heating formulation at wavelengths longward of 200 nm, and that at wavelengths shortward of 200 nm from the photolysis modules mentioned above. EUV and X-ray radiation causes photoionization and generates energetic photoelectrons, and the heating due to the energetic photoelectrons is calculated following *Solomon and Qian* [2005]. For both the chemistry and radiative heating calculations, the wavelength dependent solar irradiance is parameterized in terms of the solar 10.7 cm radio flux (f10.7). The f10.7 fluxes used in the simulations are 200, 144 and 70 ($\times 10^{-22} Wm^{-2}Hz^{-1}$, or sfu) for solar maximum, medium and minimum conditions, respectively. The electron and ion energy equations are not solved in the current WACCM-X model, and the ion and electron temperatures are assumed equal to the neutral temperature. As a result, the heating of the neutral atmosphere by collisions with thermal electrons and ions are absent.

[12] The gravity wave parameterization used in WACCM-X is the same as that in WACCM3, which is based on the linear saturation theory [*Lindzen*, 1981; *Garcia et al.*, 2007]. It should be emphasized that this parameterization takes into account the damping of the gravity waves by molecular viscosity, which becomes increasingly stronger in the thermosphere.

[13] In WACCM3 and WACCM-X, the ion drag and Joule heating are calculated according to *Dickinson et al.* [1981] and *Roble et al.* [1982], respectively. The electric field, required by the ion drag and Joule heating calculations, is parameterized according to *Weimer* [1995] and *Richmond et al.* [1980] at high latitudes and middle-low latitudes, respectively. At high latitudes, the ionization rate, particle precipitation over polar cap and cusp region and neutral heating associated with aurorae are calculated using an analytical auroral model by *Roble and Ridley* [1987], as in the TIME-GCM. The input of the parameterization is the hemispheric power (HP) of precipitating auroral electrons. Both the HP and the Weimer model depend on the K_p geomagnetic index [*Maeda et al.*, 1989]. All simulations discussed in this paper are under geomagnetically quiet conditions, with K_p set to 0.33, the lowest nonzero K_p value. In the current model, electrodynamics processes (e.g., wind dynamo) are not self-consistently resolved.

[14] WACCM-X has extended the top boundary of WACCM3 from the lower thermosphere (4.5×10^{-6} hPa, or ~145 km) to the upper thermosphere (2.5×10^{-9} hPa, or

~500 km). As in NCAR TIME-GCM, this altitude is chosen because it is where the mean free path of atmospheric atoms is approximately equal to the scale height, above which it may become necessary to treat the atmosphere using kinetic theory. Below the homopause, the atmosphere is well mixed by turbulence, such that the mean molecular mass is a constant and it is only necessary to consider the eddy and molecular diffusion of minor species in a uniform background atmosphere. This becomes problematic as diffusive separation becomes important above the homopause, and it is necessary to properly treat the molecular diffusion of the major species (N_2, O_2, and O), as well as the dependence of molecular mass, specific heats, and coefficients of molecular viscosity, thermal and species diffusion on the variable composition. In WACCM-X, these are taken into account in the physics modules. The major species molecular diffusion is included using the formulation proposed by *Dickinson et al.* [1984], which is used in TIME-GCM. The mean molecular mass $\overline{m}$ and quantities dependent on the molecular mass (e.g., the gas constant $R = k/\overline{m}$, where k is the Boltzmann constant) are calculated as a function of the mixing ratio of the major species. The specific heats at constant pressure and constant volume, c_p and c_v, respectively, are calculated as [*Banks and Kockarts*, 1973]

$$c_p = \sum_i \frac{k}{m_i}\left(1 + \frac{N_i}{2}\right)\phi_i \tag{1}$$

$$c_v = \sum_i \frac{k}{m_i}\frac{N_i}{2}\phi_i \tag{2}$$

where i is for one of the 3 major species, N_2, O_2, and O, $N_O = 3$, $N_{O_2} = N_{N_2} = 5$, m_i and ϕ_i are the molecular mass and mass mixing ratio for the ith species. It is evident from equations (1) and (2) that the specific heats decrease with altitude in the thermosphere as O becomes more abundant. The molecular viscosity and thermal conductivity (μ and η) are [*Banks and Kockarts*, 1973]

$$\mu = (4.03\phi_{O_2} + 3.42\phi_{N_2} + 3.9\phi_O)T^{0.69}10^{-7}\ \mathrm{kg\,m^{-1}\,s^{-1}} \tag{3}$$

$$\eta = (56(\phi_{O_2} + \phi_{N_2}) + 75.9\phi_O)T^{0.69}10^{-5}\ \mathrm{J\,m^{-1}\,K^{-1}\,s^{-1}} \tag{4}$$

where T is neutral temperature. The impact of molecular viscosity and thermal conductivity on unit mass is proportional to the ratios μ/ρ (kinematic viscosity) and η/ρ (ρ is the mass density of the neutral atmosphere), respectively. With the mass density decreasing exponentially and temperature increasing with altitude, the molecular viscosity and thermal conduction are dominant in the upper thermosphere. In the current model, the molecular viscosity and diffusion are only considered in the vertical direction. This does not pose a serious problem with the current model resolution, because the resolvable horizontal scales are much larger than the resolvable vertical scales, and that diffusion is inversely proportional to the square of the spatial scales. The molecular diffusion coefficient for the jth minor species is

$$D_j = \frac{\sqrt{T}}{\rho}\overline{m}\sqrt{\left(\frac{1}{\overline{m}} + \frac{1}{m_j}\right)\frac{1}{Av}}1.52 \times 10^{20}\ \mathrm{m^2 s^{-1}} \tag{5}$$

where Av is Avogadro's number. These coefficients also become increasingly large in the thermosphere.

[15] Most of the atmospheric species are in diffusive equilibrium, and the vertical gradients of temperature and winds are approximately zero in the upper thermosphere, due to the large molecular diffusion and viscosity. These can be used as the upper boundary conditions for these quantities, and they eliminate the need to specify the upper boundary condition using TIME-GCM or empirical models as was done in the standard WACCM. An exception is the atomic hydrogen, whose escape flux is considered. In the WACCM-X model presented here, only a uniform flux of $10^{12}\mathrm{s^{-1}m^{-2}}$ for atomic hydrogen is applied. A more elaborate formulation of Jean's escape flux [e.g., *Walker*, 1977] will be implemented in future versions of the model.

[16] With the extension of the vertical domain to the upper thermosphere, the number of vertical levels is increased from 66 to 81. The vertical resolution in the extended domain is half of a scale height, the same as in the mesosphere and lower thermosphere. The vertical domain has also been configured and tested with a vertical resolution of one-quarter scale height above 1 hPa, with 125 vertical levels. The horizontal resolution used in the WACCM-X simulations presented here is 1.9° × 2.5° (latitude × longitude). As in CAM3 and WACCM3 using finite volume dynamics, a time-splitting scheme is used: one time step for the integration of tracer transport equations and physics and a much smaller time step for the dynamics equations to stabilize the fastest waves. In WACCM-X simulations, the former needs to be reduced from 30 minutes, which is standard for CAM3 and WACCM3, to 5 minutes, and the smaller time step for dynamics integration is 50 seconds. This is because of the short temporal scales of thermospheric processes. As in the CAM3 and WACCM3, longitudinal filtering is used in the polar region to remove the smaller spatial scales to maintain numerical stability.

3. Model Results

[17] The model is evaluated here through its capability to represent the compositional, thermal and wind structures, the seasonal variation of the thermosphere, migrating and nonmigrating tides and their seasonal variation, and the short-term variability in the thermosphere due to coupling with the lower atmosphere. The evaluation is performed by comparing WACCM-X results with satellite observations, NCAR upper atmosphere Global Mean Model [*Roble*, 1995], Thermosphere-Ionosphere-Electrodynamics general circulation model (TIE-GCM) [*Richmond et al.*, 1992], and Mass-Spectrometer-Incoherent-Scatter (MSIS) model [*Picone et al.*, 2002]. The model tides are also compared with NOAA WAM results, because the tides from WAM have been favorably compared with TIMED/SABER observations. It is noted that WAM covers the same vertical domain as WACCM-X (ground to the upper thermosphere at ~10^{-9} hPa), and is based on a dynamical core different from WACCM. The results presented here are based on three one-model-year simulations, with each one under generic climate conditions and constant solar conditions (f10.7 set to 200, 144, and 70 sfu as mentioned above). A one-year spin-up simulation was performed to create the initial condition for these simulations. The specification of the sea surface

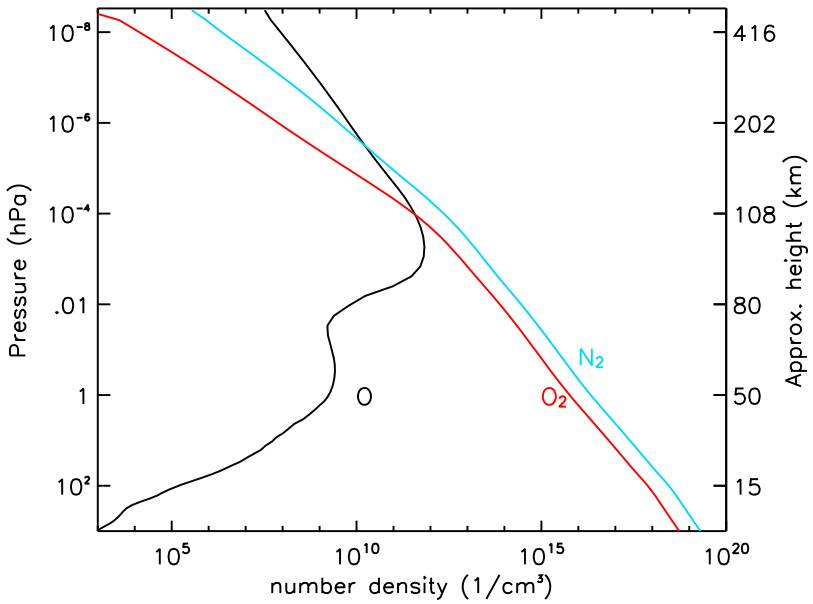

Figure 1. Number densities of major neutral species averaged over December and globally from WACCM-X simulations under solar medium conditions.

temperature and the mixing ratio of various chemical species are described by *Garcia et al.* [2007].

3.1. Compositional Structures

[18] Figure 1 shows the vertical number density profiles of the major neutral species, N_2, O_2 and O, from the Earth's surface to the upper thermosphere as resolved by WACCM-X. These are global mean profiles obtained from WACCM-X results under December solstice and solar medium conditions. They are in excellent agreement with those obtained from the upper atmosphere Global Mean Model between 10 and 3×10^{-9} hPa (the vertical range of the Global Mean Model). For example, in both models, as well as in MSIS, the altitudes where [O] is equal to $[O_2]$ and $[N_2]$ are at $\sim 10^{-4}$ hPa (110 km, at the turbopause) and $\sim 1.5 \times 10^{-6}$ hPa (170 km), with number densities at 2×10^{11} and 10^{10} cm^{-3}, respectively (cm^{-3} is used in the plots and the discussions here, so that the number densities are directly comparable with the Global Mean Model results). The global mean profiles of oxygen compounds (O, O_3, $O(^1D)$, $O_2(^1\Delta)$, and $O_2(^1\Sigma)$), hydrogen compounds (H, H_2, H_2O, OH, and HO_2), nitrogen compounds (NO, NO_2 and N_2O), and carbon compounds (CO, CO_2, and CH_4) from WACCM-X are given in Figure 2. Most of them show good general agreement with the Global Mean Model results, although CO decreases faster with altitude than in the Global Mean Model above ~100 km. The global mean density profiles of 5 main ions (O^+, O_2^+, NO^+, N^+, and N_2^+) and electrons are shown in Figure 3. From Figure 3, the global mean electron density is $\sim 5 \times 10^4$ cm^{-3} in the E region and $\sim 10^6$ cm^{-3} at the F2 peak at 10^{-7} hPa (~250 km). These are in good agreement with those from the Global Mean Model up to the F2 peak. However, the number densities decrease much faster than those from the Global Mean Model, and this is likely due to the lack of ambipolar diffusion in the current model. As a result, the ionospheric structures in the current model are not realistically resolved.

[19] $[O]/[N_2]$ is a quantity used to gauge the relative abundance of atomic and molecular species in the thermosphere. It has been found that $[O]/[N_2]$ in the thermosphere has a semiannual variation, with maximum at equinox and minimum at solstice. This semiannual variation, according to *Fuller-Rowell* [1998], is due to the "thermospheric spoon" effect: the interhemispheric circulation at solstice acts to enhance the mixing of thermospheric species and reduces the diffusive separation. As a result, the mixing ratio of atomic oxygen decreases and the mixing ratios of molecular nitrogen and oxygen increase, so that $[O]/[N_2]$ decreases at solstice. The semiannual variation is reproduced in the WACCM-X simulation. Figure 4 shows the monthly mean $[O]/[N_2]$ under solar maximum, medium, and minimum conditions. The semiannual variation of $[O]/[N_2]$ can be seen in all these simulations (pressure level 1.8×10^{-7} hPa is chosen to be comparable with Figure 3 of *Fuller-Rowell* [1998], which shows $[O]/[N_2]$ at 1.73×10^{-7} hPa from MSIS). The ratio varies between 6 and 8, 5 and 7, and 4 and 5 for solar maximum, medium and minimum conditions, respectively. The magnitude and seasonal variation of the ratio under solar medium conditions compares well with those from MSIS under similar solar conditions and geomagnetically quiet conditions [*Fuller-Rowell*, 1998]. The dependence of the $[O]/[N_2]$ on solar activity, as seen in Figure 4 and in MSIS, likely reflects the temperature dependence of molecular diffusion. According to equation (3), the molecular diffusion increases with temperature (thus solar activity), which enhances the molecular diffusion and thus the relative abundance of the atomic species in the thermosphere.

[20] Although the semiannual variation of $[O]/[N_2]$ in the thermosphere is reasonable in the model, the semiannual variation of air density above 200 km [*Paetzold and Zschorner*, 1961; *Bowman*, 2004] is not reproduced. The global mean mass density on fixed heights from the model only shows semiannual variation between ~90–160 km. The largest relative density variation is at ~110 km, with the

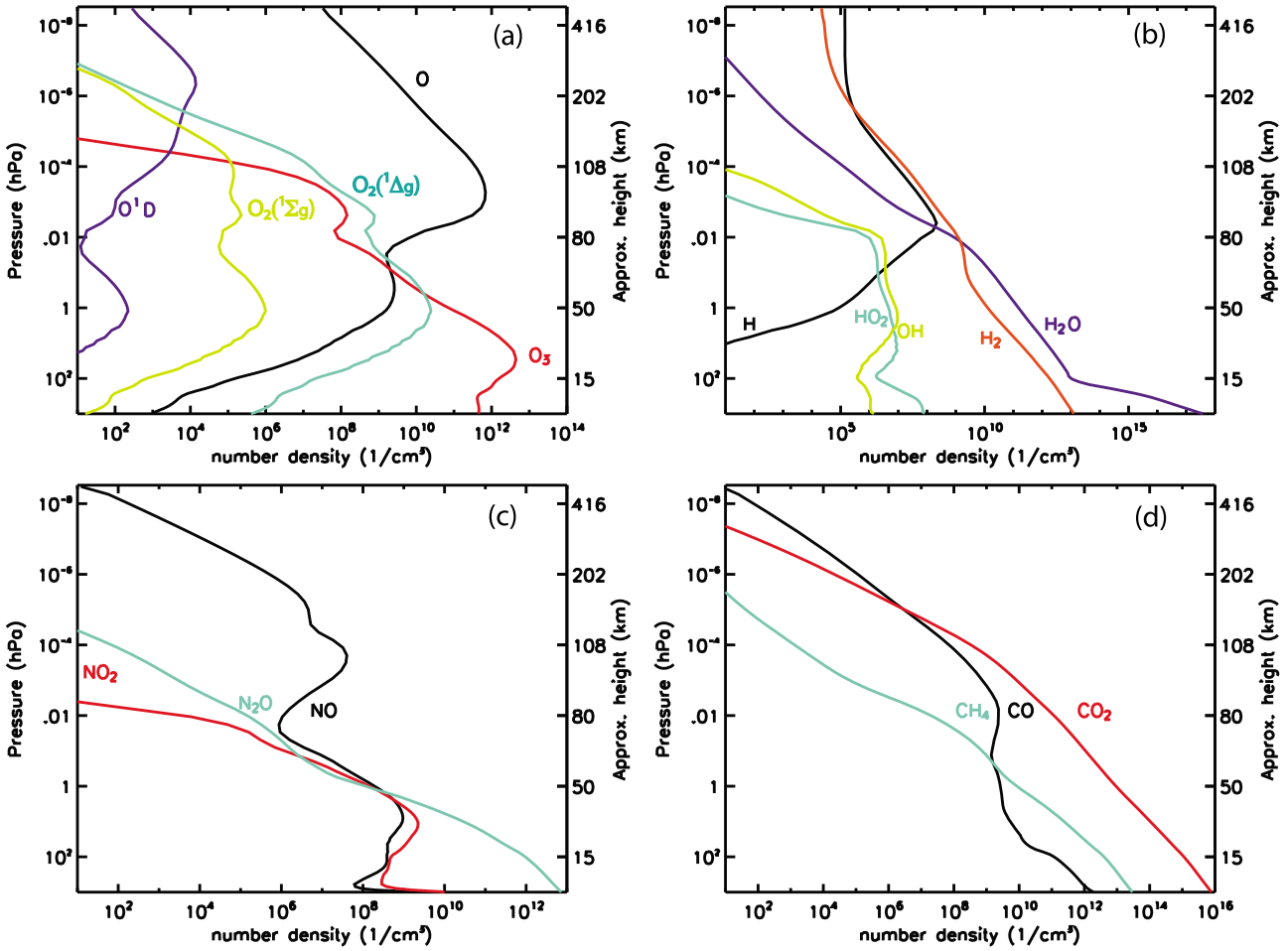

Figure 2. Number densities of (a) oxygen, (b) hydrogen, (c) nitrogen, and (d) carbon compounds averaged over December and globally from WACCM-X simulations under solar medium conditions.

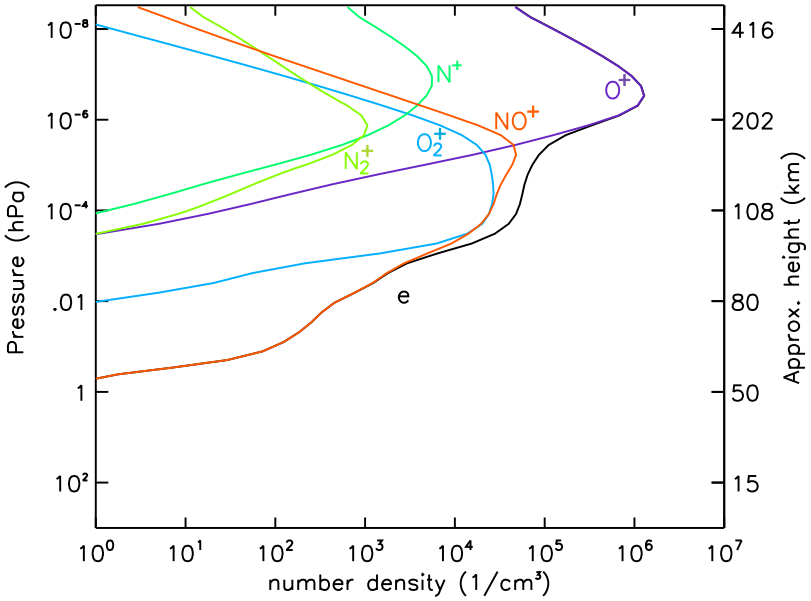

Figure 3. Number densities of ions and electrons averaged over December and globally from WACCM-X simulations under solar medium conditions.

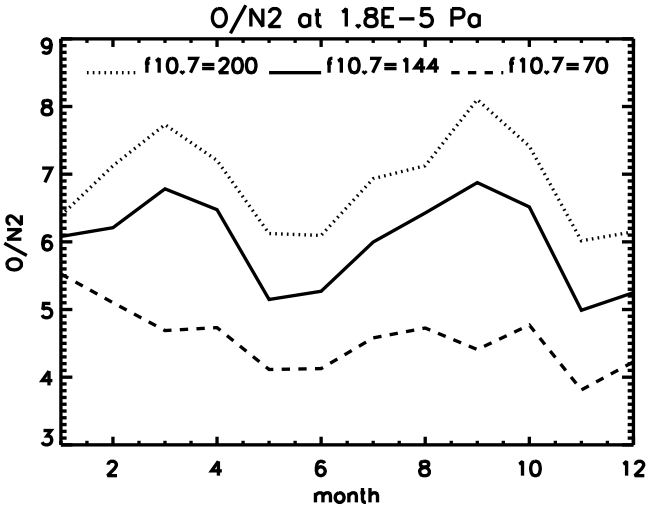

Figure 4. Globally averaged $[O]/[N_2]$ at 1.8×10^{-7} hPa under solar maximum (dotted line), solar medium (solid line), and solar minimum (dashed line) conditions.

density in March and October ~15% above the annual average, and the density in July and January ~23% and ~5% below the annual average, respectively. Above 160 km, the global mean density from the model only displays an annual variation, with the maximum around December and the minimum around May (in the upper thermosphere 11% and 8% above and below the annual average, respectively).

3.2. Temperature and Wind Structures

[21] Figure 5 shows the monthly averaged zonal mean temperature, zonal wind, meridional wind, and mass stream function from a WACCM-X simulation for December under solar medium conditions. The stream function is calculated according to residual mean meridional and vertical winds [e.g., *Andrews et al.*, 1987]. It should be noted that the residual mean winds calculated according to the transformed Eulerian mean formulation are almost identical to the zonal mean winds in the thermosphere. This is because the mean momentum and heat fluxes associated with large-scale waves become less important in the upper atmosphere than in the middle atmosphere, when the gravity wave driving becomes dominant in the mesosphere and then most of the propagating waves are damped in the thermosphere. The lower and middle atmosphere structures are reasonably captured, as discussed in detail by *Garcia et al.* [2007]. In particular, the parameterized gravity wave forcing drives the mesosphere and lower thermosphere from radiative equilibrium, leading to a summer-to-winter temperature gradient between ~60–110 km. The minimum temperature of ~130 K is located at ~85 km above the South (summer) Pole, and the mesopause height in the Southern (summer) hemisphere decreases toward the equator. The mesopause heights in the Northern (winter) hemisphere and at low southern latitudes are at about 100 km and the mesopause temperature is about 200 K. These features are in agreement with TIMED/SABER observations [*Xu et al.*, 2007], although the mesopause temperature of 200 K is warmer than those obtained from SABER (180–190 K). This discrepancy was also found when comparing WACCM with lidar measurements [*Yuan et al.*, 2008]. According to recent numerical experiments, the excessive dissipative heating from the gravity wave parameterization scheme is largely responsible for this warm temperature in the model (C.-C. Chen, personal communication). In the thermosphere, the temperature increases rapidly up to 200 km and becomes approximately isothermal in the upper thermosphere due to the large molecular heat conduction. Stronger heating in the summer hemisphere leads to a large temperature gradient from the winter hemisphere to the summer hemisphere.

[22] The gravity wave forcing causes zonal wind reversal in the mesosphere, which is properly resolved by the model. According to the model results, the zonal wind reversal extends from about 70 km (0.02 hPa, low latitude) or 95 km (0.001 hPa, high summer latitude) to 120 km (3×10^{-5} hPa) and is in a similar altitude range as that of the temperature gradient reversal. This is in general agreement with the wind climatology from measurements by the High Resolution Doppler Instrument (HRDI) and the Wind Imaging Interferometer (WINDII) on board the Upper Atmosphere Research Satellite (UARS) and climatology from the UARS Reference Atmosphere Project (URAP) [*McLandress et al.*, 1996; *Swinbank and Ortland*, 2003]. Detailed comparison of the wind climatology up to the lower thermosphere between WACCM (which has the same physics as WACCM-X below 140 km) and URAP is given by *Garcia et al.* [2007]. In the upper thermosphere, the zonal wind is eastward in the low and middle latitudes and becomes westward at high latitudes, with the maximum wind at midlatitudes in the winter hemisphere. This agrees with the climatology of the thermospheric wind [e.g., *Fuller-Rowell*, 1995; *Drob et al.*, 2008]. The thermospheric wind is driven by a combination of differential solar heating, differential magnetospheric heating, and ion drag [*Fuller-Rowell*, 1995]. The zonal mean ion drag at low latitudes is eastward above ~200 km and increases with altitude. It can exceed 800 $ms^{-1}d^{-1}$ near the model top (similar for equinox conditions), and may play an important role in driving the superrotation. It should be noted, however, that the ion drag from the model is inaccurate because the ion density there is not accurately modeled as mentioned earlier.

[23] Strong summer to winter circulation patterns are seen in the mesosphere (60–90 km) and the thermosphere (above ~120 km) (Figures 5b and 5c). The former is driven primarily by gravity wave forcing, and the latter by the large gradient of heating between summer and winter hemispheres. The maximum mean meridional wind in the upper thermosphere is in the winter hemisphere, consistent with the zonal wind. A winter to summer circulation is seen in the lower thermosphere (90–120 km), which is connected to summer to winter circulation in the thermosphere and in the upper mesosphere according to the mass stream function.

[24] Figure 6 shows the monthly averaged zonal mean temperature, zonal wind, meridional wind, and mass stream function for March. The temperature and winds are more symmetric with respect to the equator, but not perfectly so due to lag in the atmospheric responses. The temperature extremum near 100 km from WACCM-X is ~210 K, warmer than the mesopause temperature measured by SABER and from TIME-GCM (~180 K). This extremum at 100 km is close to, and sometimes smaller than the extremum at 80 km, so that the location of the minimum tem-

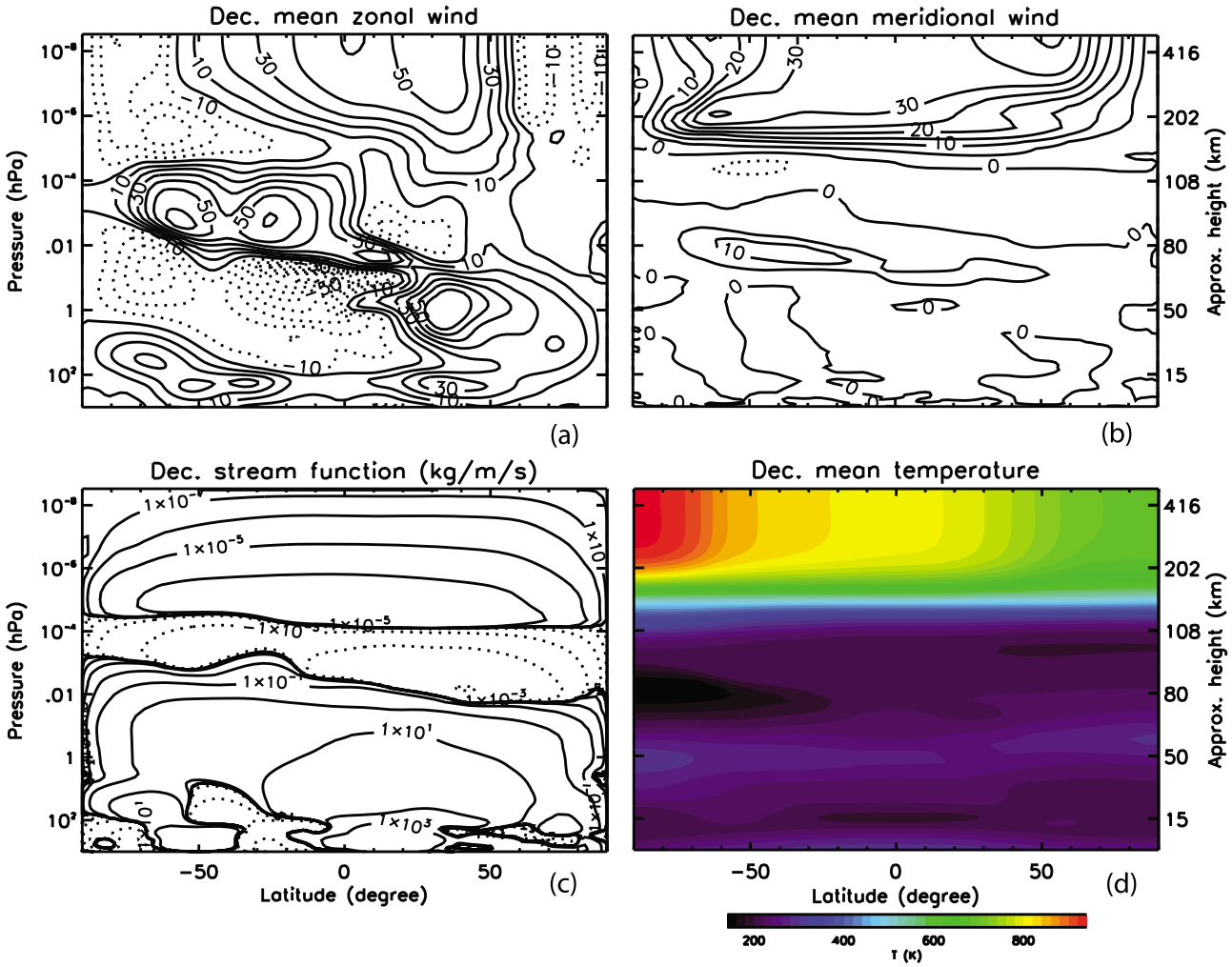

Figure 5. Monthly averaged zonal mean (a) zonal wind, (b) meridional wind, (c) mass stream function, and (d) temperature for December. Contour intervals: 10 ms^{-1} (solid: eastward) for Figure 5a, 2.5 ms^{-1} (solid: northward) for Figure 5b, and log scale and by one decade (unit: kg $m^{-1}s^{-1}$) for Figure 5c.

perature (i.e., mesopause height) may go down to 80 km. According to SABER observations, however, the mesopause height should be near 100 km at March equinox. As mentioned earlier, this is due to the excessive dissipative heating from the gravity wave parameterization.

[25] The mean zonal wind agrees with the URAP wind climatology in the MLT. The vertical variation from the eastward wind starting from stratopause to westward wind at the mesopause is a feature due to the semiannual oscillation (SAO), although it is weaker than the observed SAO [*Richter and Garcia*, 2006]. The thermospheric zonal wind is quite consistent with climatology from the empirical model [*Fuller-Rowell*, 1995; *Drob et al.*, 2008]: at low to mid latitudes the zonal wind is weakly eastward in the lower thermosphere, strongly eastward in the upper thermosphere (superrotation), and weakly westward in between. The wind is westward at high latitudes due to auroral forcing. The superrotation, however, is not seen in the HRDI/WINDII climatology or in the TIME-GCM simulation [*McLandress et al.*, 1996; *Roble*, 2000]. The zonal mean meridional wind and the mass stream function show an alternating poleward and equatorward pattern from the mesosphere to the upper thermosphere, which is similar to those from the empirical model, HRDI/WINDII climatology and TIME-GCM, although the magnitude of the wind is smaller than those in the HRDI/WINDII climatology and TIME-GCM. Above ~190 km, the northward meridional circulation appears to be more extensive. This is because the transition from northward to southward circulation occurs at equinox, and monthly averaging weighs pretransition period (20 days) more than the posttransition period (10 days).

3.3. Longitudinal Variation and Tides

[26] Atmospheric temperature, winds and composition are characterized by spatial and temporal variations. In the upper atmosphere, these variations are determined by tides, planetary waves, gravity waves, and solar and magnetospheric driving. As mentioned earlier, the solar and magnetospheric driving are held constant in the WACCM-X simulations presented here, and the magnetospheric condition is very quiet. Therefore, the variations discussed here are mainly from the lower atmosphere perturbations and thermal tides. Figure 7 shows the neutral temperature in the lower thermosphere (2.7×10^{-5} hPa, ~125 km) and upper

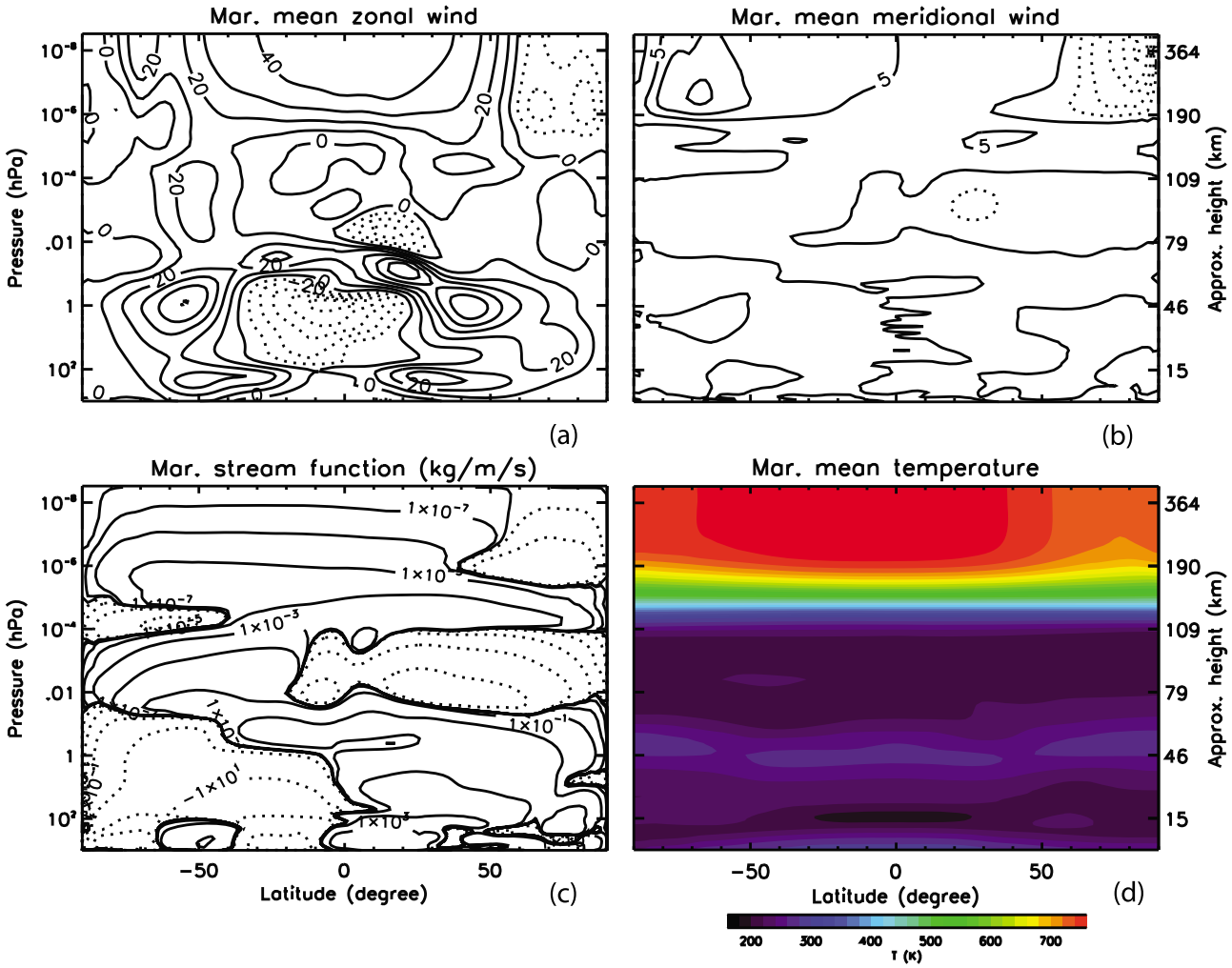

Figure 6. Similar to Figure 5, but for March.

thermosphere (6.6×10^{-8} hPa, ~290 km) on day 80 (March equinox) at UT 0 under solar maximum conditions. In the lower thermosphere, the temperature from WACCM-X varies with longitude and latitude. The most visible patterns are wavenumber 3 near the equator and wavenumber 2 at midlatitudes. The wavenumber 2 structure is mainly from the migrating semidiurnal tide, and is also the dominant longitudinal pattern in MSIS and the TIE-GCM. The wavenumber 3 structure comes from the diurnal eastward 3 (DE3) nonmigrating tide, which is not present in MSIS or TIE-GCM. It should be noted that the lower boundary of TIE-GCM at ~97 km is specified by the Global Scale Wave Model (GSWM) [*Hagan et al.*, 1999], and in the simulations presented here only migrating tides are specified. The temperature in the upper thermosphere shows a dominant diurnal (wavenumber 1) pattern, which is primarily driven by solar heating. The temperature peaks in the afternoon (near LT1600 or 120°W) and is the coldest after midnight (0° longitude), which is in general agreement with MSIS and TIE-GCM. Superposed upon the diurnal variation, the temperature clearly shows a local maximum after midnight. The area with the local maximum tilts poleward-eastward, which translates to a poleward spread with local time. The temperature difference between this local maximum and the lowest temperature ~60° to the east (~3 hours later in local time) is about 80 K at the equator. These features are consistent with the observed thermospheric midnight temperature maximum (MTM) [*Harper*, 1972; *Herrero and Spencer*, 1982]. Furthermore, the poleward-eastward tilting is also seen around the temperature peak in the afternoon (120°W). Recent studies using whole atmospheric models have identified the MTM and related it to superposition of tidal perturbations, including those excited by the terminator waves, and have shown that MTM displays seasonal and day-to-day variability [*Akmaev et al.*, 2008; *Miyoshi et al.*, 2009; *Fujiwara and Miyoshi*, 2010]. It is noted that the temperature from WACCM-X is lower than the temperature from TIE-GCM and MSIS: by about 200 K and 150 K near the temperature maximum and minimum, respectively. As mentioned earlier, since the electron and ion temperatures are the same as the neutral temperature in the current model, the heating of neutral atmosphere through collisions with thermal electrons and ions is not considered. Because this is one of the dominant heating sources of the neutral atmosphere above ~250 km [*Rees and Roble*, 1975; *Roble*, 1995], its absence may be responsible for the temperature

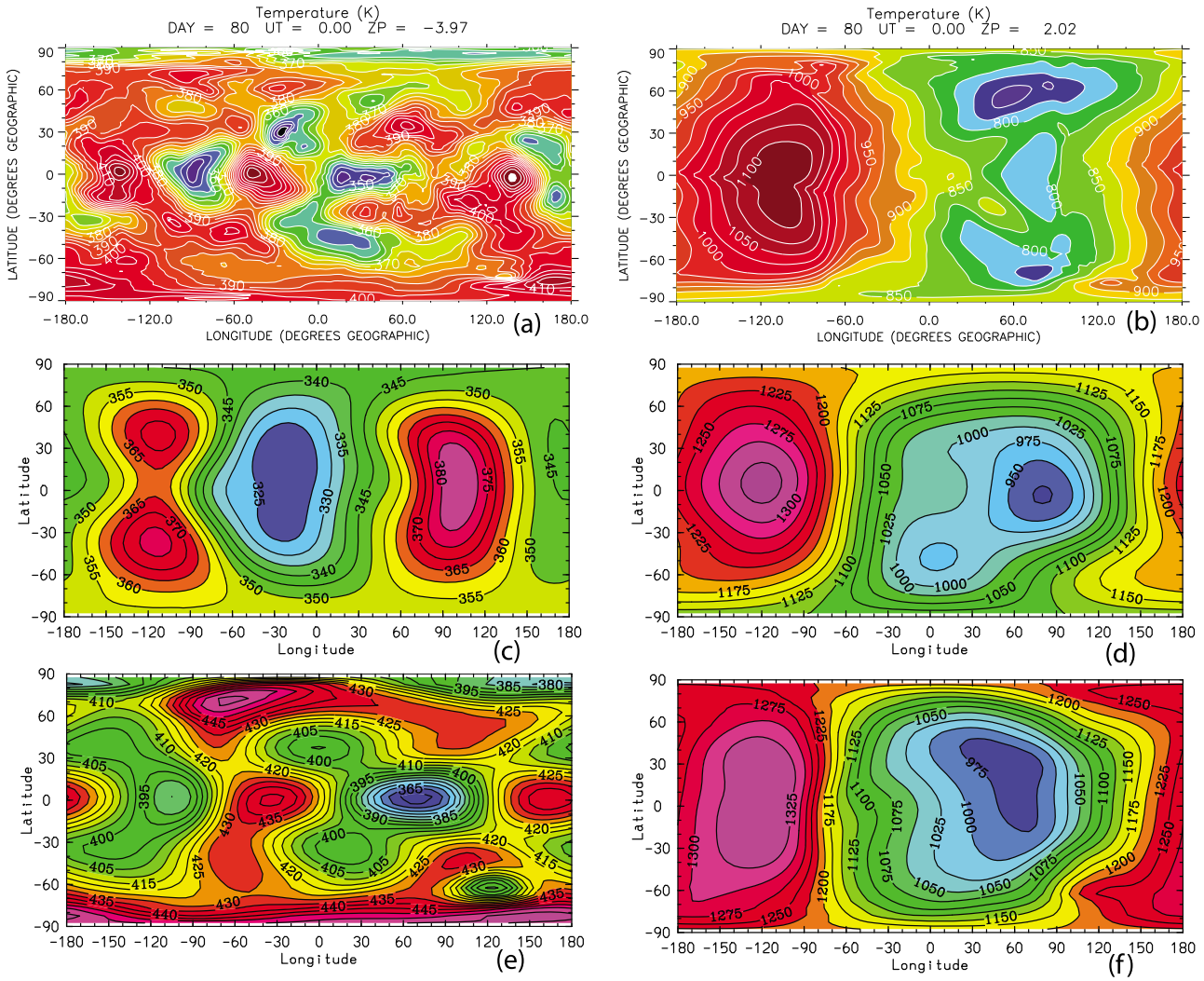

Figure 7. Neutral temperature in the (left) lower thermosphere (2.7×10^{-5} hPa, ~125 km) and (right) upper thermosphere (6.6×10^{-8} hPa, ~290 km) at March equinox. (a and b) WACCM-X simulation, (c and d) MSIS, and (e–f): TIE-GCM. Contour intervals: 5K in Figures 7a, 7c and 7e; 25K in Figures 7b, 7d, and 7f.

discrepancy between WACCM-X and TIE-GCM and MSIS.

[27] Figure 8 shows the amplitude of the migrating diurnal tide of temperature at 0.004 hPa (~85 km), derived from the monthly averaged daily variation, under solar medium conditions. The migrating diurnal tides under different solar conditions are very similar at this altitude. The tidal amplitude peaks at equinoxes, with the primary peak at March equinox. The seasonal variation, as well as the meridional structure of the tide, is in good agreement with that derived from SABER measurements [*Zhang et al.*, 2006; *Garcia*, 2009]. The peak amplitude of 13 K from the model, however, is smaller than the peak value of 16 K from multiple years of SABER measurements at the same altitude. Figure 9 shows the amplitude of the monthly mean migrating diurnal tides of zonal and meridional winds at 8.8×10^{-4} hPa (~95 km) under solar medium conditions. Their seasonal and latitudinal variations compare well with those obtained from TIDI [*Wu et al.*, 2008a]. As in the case of the temperature component, the peak amplitudes are smaller than the tides from the observations. The latitudinal structure of the migrating diurnal tide at this altitude is similar to that obtained from the NOAA WAM for July [*Fuller-Rowell et al.*, 2008], but the amplitude from WACCM-X is weaker.

[28] From additional WACCM-X simulations, it is found that the amplitude and phase of the migrating diurnal tide in the MLT region are affected by the vertical resolution of the model. The migrating diurnal tidal amplitude of temperature from WACCM-X with 81 levels (corresponding to about half scale height resolution in the mesosphere and thermosphere) is systematically smaller compared with that from WACCM-X with 125 levels (quarter scale height resolution) at March equinox. The vertical wavelength of the migrating diurnal tide is about 24 km in these simulations, which contains 7–8 grid levels with half scale height resolution in the mesosphere. The smaller wave amplitude in the former case thus may in part be caused by insufficient vertical resolution. Parameterized gravity wave forcing can also affect tidal amplitudes in the MLT. Using the Lindzen

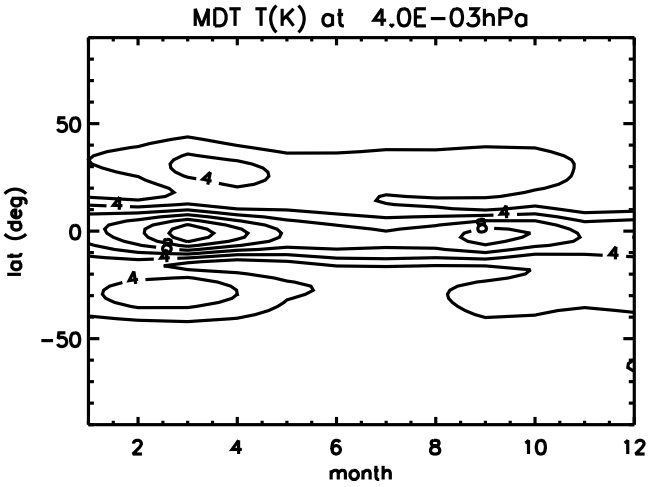

Figure 8. Monthly mean migrating diurnal tide of temperature at 0.004 hPa (~85 km) under solar medium conditions. Contour interval: 2K.

type scheme, an increase of gravity wave amplitudes tends to decrease the tidal amplitudes.

[29] The strength of the diurnal, eastward propagating, wavenumber 3 nonmigrating tidal component (DE3) has an amplitude that is comparable to the diurnal migrating tide in the lower thermosphere. Figure 10 shows the temperature and zonal wind amplitudes of this component in the MLT region. The maximum amplitudes are found around the September equinox, with a temperature amplitude at 13 K and zonal wind amplitude at 17 ms^{-1}. The location of the temperature peak is slightly to the south of the equator, and the location of the zonal wind peak is slightly to the north. These features are in good agreement with those obtained from SABER [*Zhang et al.*, 2006; *Garcia*, 2009] and TIDI [*Wu et al.*, 2008b] at the same heights. These observations show that the DE3 peaks between August and October with a temperature amplitude of ~14 K located slightly to the south of the equator, and zonal wind amplitude of 16 ms^{-1} located slightly to the north of the equator. Figure 11 compares the vertical profiles of DE3 zonal wind amplitude and phase (averaged over ±5° latitude) for August obtained from TIMED SABER and TIDI using a Hough Mode Extension (HME) fitting method [*Oberheide and Forbes*, 2008] and WACCM-X. The DE3 from HME are average values for the years 2002–2005 with mean solar f10.7 of 128 sfu (HME DE3 from individual years are given by *Oberheide et al.* [2009]). The averaging over the four years is necessary to remove the QBO signal. The amplitudes are in excellent agreement up to 100 km, where the DE3 zonal wind amplitude from HME peaks at 20 ms^{-1}. The simulated DE3 grows further till it reaches the maximum of 25 ms^{-1} at 110 km. The tidal phase (Figure 11, right) also suggests that the modeled wave maintains its propagating character to higher altitudes. Therefore, the modeled DE3 is being dissipated less strongly in the altitude range 105–180 km than implied by the observations. Above 180 km, the DE3 zonal winds from both HME and WACCM-X drop to 4–6 ms^{-1}, consistent with the DE3 zonal wind derived from the measurements by the Challenging Minisatellite Payload (CHAMP) satellite [*Oberheide et al.*, 2009; *Häusler et al.*, 2010]. The vertical wavelength of DE3 from the observation is ~45 km and the model result is ~42 km in the MLT. This difference in the vertical wavelength is reflected in the small phase difference of DE3 between the HME and WACCM-X in 60–100 km. The phase difference increases above 100 km.

[30] Figure 12 shows the seasonal variation of the temperature amplitude of the migrating semidiurnal, semidiurnal westward wavenumber 1 (SW1) and westward wavenumber 3 (SW3) components at ~110 km from the WACCM-X simulation under solar medium conditions. The migrating semidiurnal tide from WACCM-X peaks at solstice, but the peak amplitude of 12 K is weaker than that obtained from SABER [*Zhang et al.*, 2006; *Akmaev et al.*, 2008] (12–14 K at 100 km and 16 K at 110 km in August). Around June solstice both WACCM-X and SABER results show the primary maximum of the wave amplitude in the southern hemisphere, but around December solstice the primary maximum from WACCM-X remains in the southern hemisphere while the maximum from SABER shifts to the northern hemisphere.

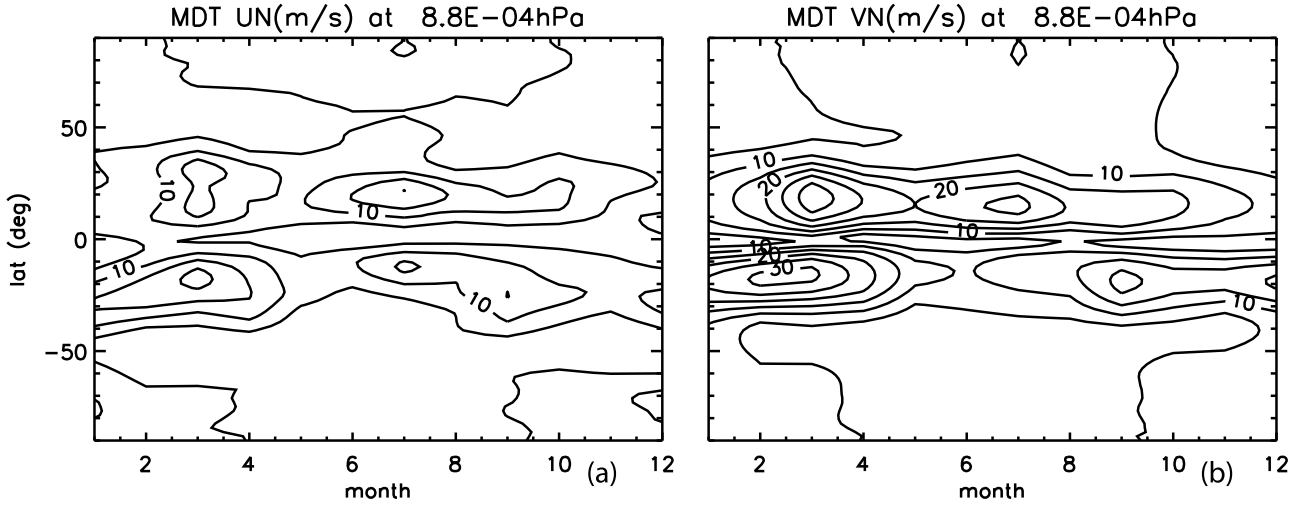

Figure 9. Monthly mean migrating diurnal tide of (a) zonal wind and (b) meridional wind at 8.8×10^{-4} hPa (~95 km) under solar medium conditions. Contour intervals: 5 ms^{-1}.

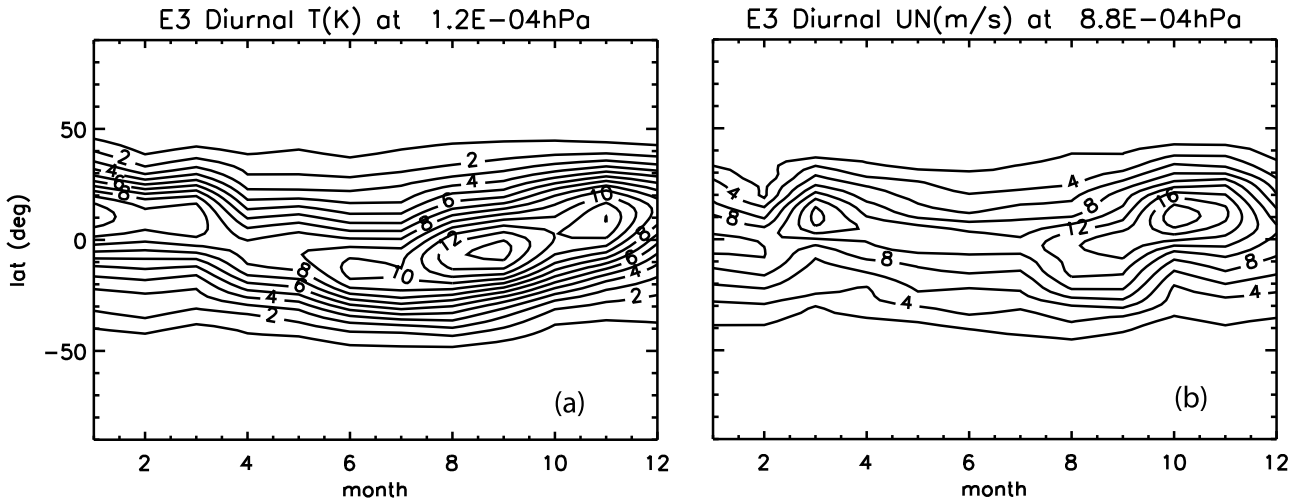

Figure 10. Monthly mean diurnal eastward propagating wavenumber 3 (DE3) tide of (a) temperature (at 1.2×10^{-4} hPa, which is near 110 km) and (b) zonal wind (at 8.8×10^{-4} hPa, which is near 95 km). Contour intervals: 1K in Figure 10a and 2 ms^{-1} in Figure 10b.

WACCM-X does poorly in reproducing the SABER SW1 component, and misses the two amplitude maxima at September and March from SABER. SW3 amplitude from WACCM-X shows a semiannual variation with peak amplitude (5 K) at 20 degree latitudes around March and October, weaker than the SW3 from SABER, which peaks around January (6 K) and September (8 K).

[31] The thermospheric tides are strongly affected by the solar heating. Figure 13 shows the migrating diurnal tide of temperature averaged over December from the ground to the upper thermosphere under solar maximum, medium, and minimum conditions. It is evident that the tide in the upper thermosphere dominates over other altitude regions. The tidal amplitudes increase rapidly with altitude in the lower to middle thermosphere, and are nearly constant with altitude in the upper thermosphere. The exact altitude of transition to the near constant amplitude varies with latitude and solar activity. The amplitudes of the migrating tides clearly increase with solar activity and peak in the summer hemisphere. WACCM-X results also show that the DE3 amplitude in the thermosphere becomes weaker with increasing solar activity (Figure 14a). At 300 km, the DE3 zonal wind amplitudes are 2, 4, and 10.5 ms^{-1} with f10.7 being 200, 144 and 70 sfu, respectively. The phase of the DE3 in the thermosphere also varies with solar activity (Figure 14b). In the upper thermosphere, the phase of DE3 shifts to earlier universal time (more westward longitude) when the solar activity increases. Because the DE3 propagation in the thermosphere is subject to damping by molecular dissipation, which increases with temperature (thus solar activity), this tidal component is subject to stronger dissipation when the solar activity increases. The stronger dissipation also increases the phase tilt of DE3 in pressure coordinates above ~10^{-4} hPa (inset plot), resulting in the phase shifts in the upper thermosphere. These model results are consistent with the findings from HME fitting to TIMED data [*Oberheide et al.*, 2009] and the DE3 zonal wind from CHAMP [*Häusler et al.*, 2010].

[32] Apart from DE3, other nonmigrating diurnal tides have also been identified in the thermosphere [*Forbes et al.*, 2008, 2009; *Häusler et al.*, 2010]. Figure 15 shows the zonal and meridional wind amplitudes of the diurnal east-

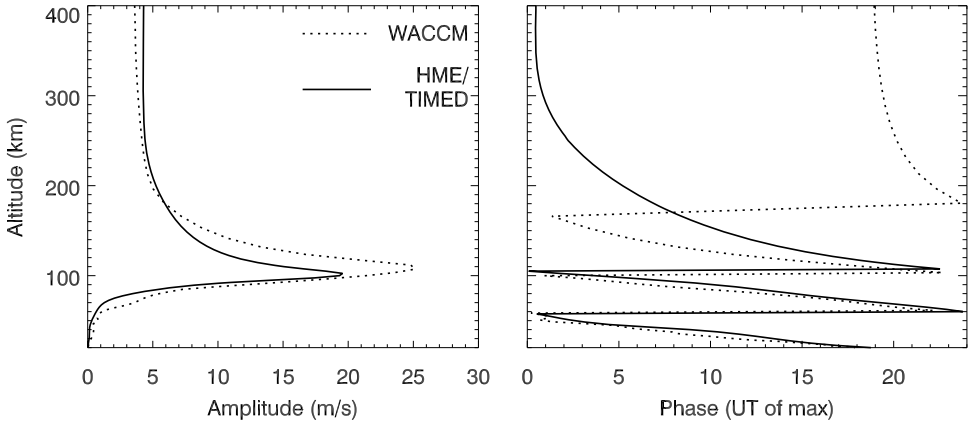

Figure 11. The (left) amplitude and (right) phase of the DE3 zonal wind for August from HME fitting to 2002–2005 TIMED data (solid line) and WACCM-X (dotted line) at the equator.

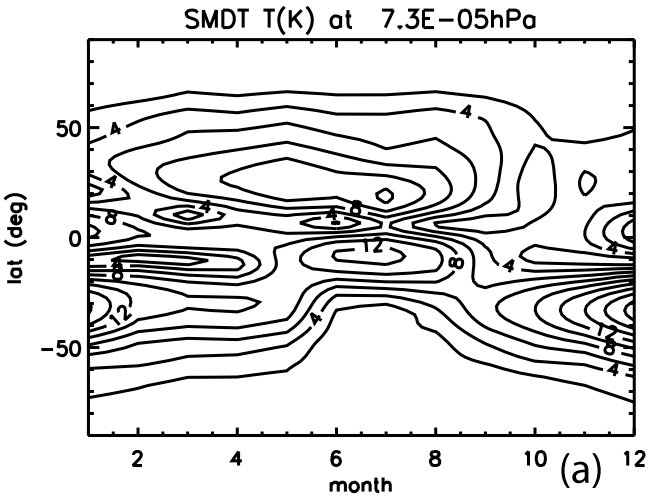

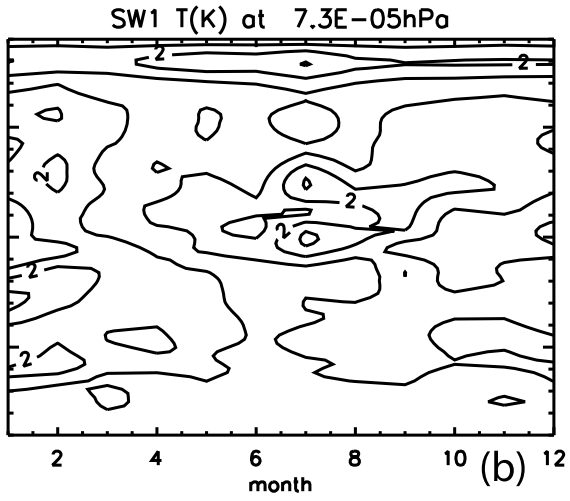

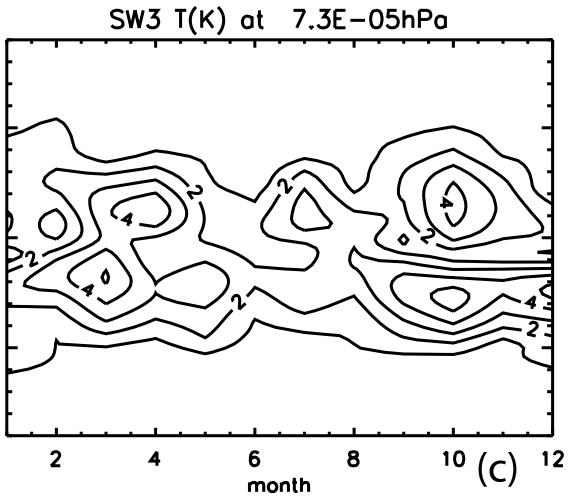

Figure 12. Monthly mean (a) semidiurnal migrating tide, (b) SW1, and (c) SW3 of temperature at 7.3×10^{-5} hPa (~110 km) under solar medium conditions. Contour intervals: 2 K.

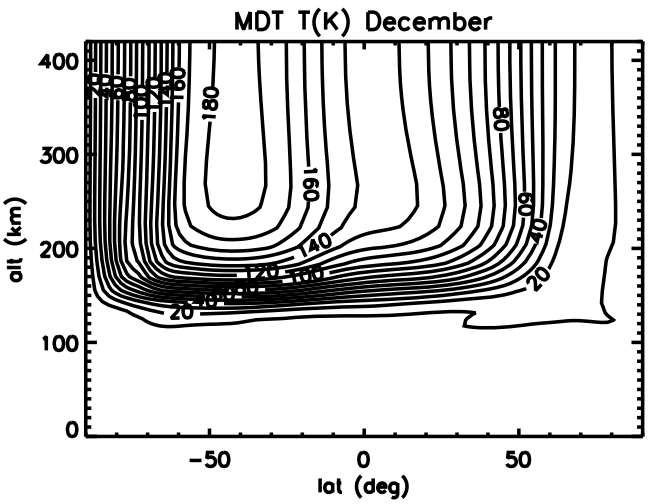

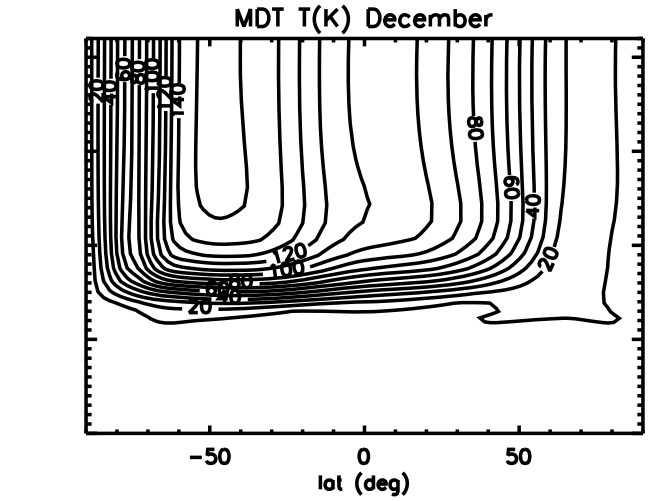

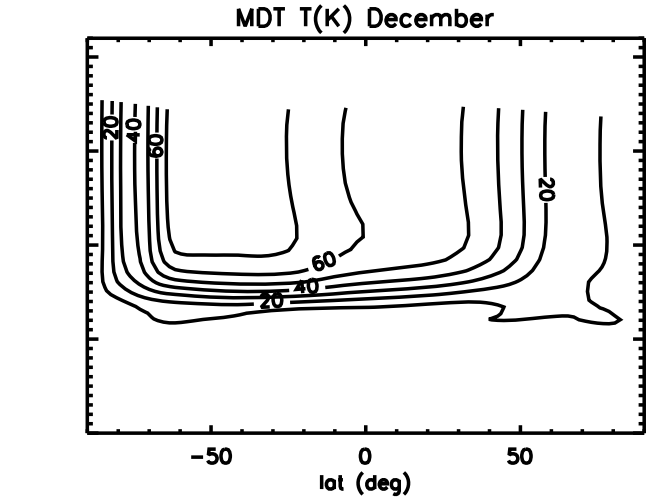

Figure 13. Migrating diurnal tide of temperature for December under (top) solar maximum, (middle) solar medium, and (bottom) solar minimum conditions. Contour intervals: 10K.

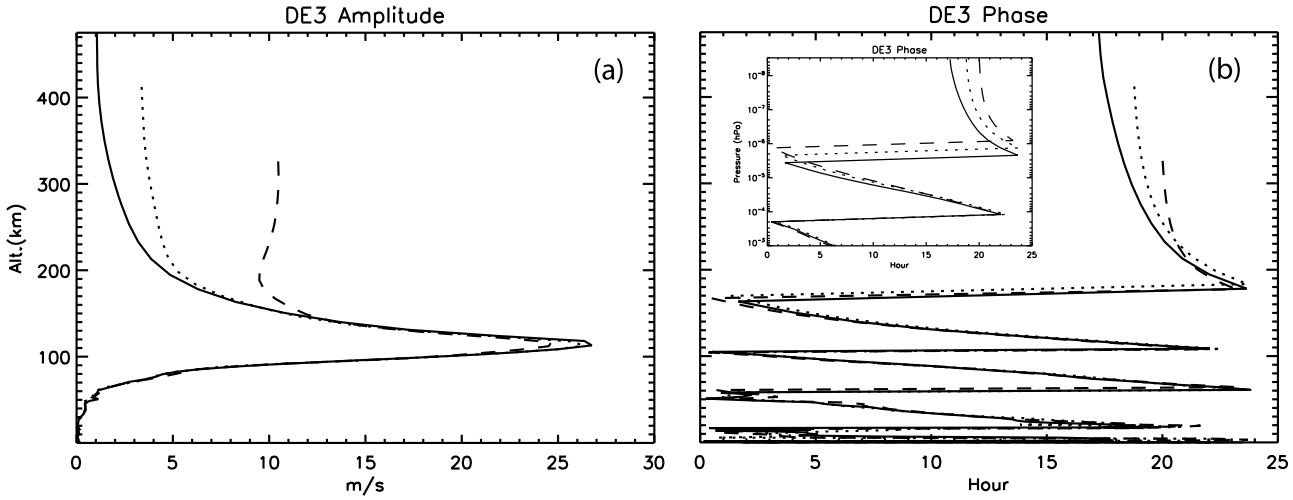

Figure 14. (a) Amplitude and (b) phase of the DE3 zonal wind component at the equator from WACCM-X simulations for F10.7 equal to 200 (solid line), 144 (dotted line), and 70 (dashed line) sfu. The inset plot in Figure 14b shows the phase in pressure coordinates.

ward wavenumber 2 (DE2), eastward wavenumber 1 (DE1), wavenumber 0 (D0), and westward wavenumber 2 (DW2) components of June from WACCM-X under solar minimum conditions. In the lower thermosphere, DE2, DE1 and D0 reach their maxima near 110 km, and DW2 maximizes at ~95 km. These heights agree with the heights of the maximum temperature amplitudes of DE2, D0 and DW2 derived from SABER [*Forbes et al.*, 2008]. In the upper thermosphere, the DE2 zonal wind peaks at the equator with an amplitude of 10 ms^{-1}, which is similar to the the DE2 zonal wind derived from CHAMP under solar minimum conditions [*Häusler et al.*, 2010]. The maximum DW2 amplitude in the upper thermosphere from WACCM-X is 14 ms^{-1}, comparable to the maximum DW2 amplitude from CHAMP, though the former is at lower latitude. The D0 amplitude from the model is larger than the CHAMP results at low latitudes. WACCM-X simulations also show that the DE2 zonal and meridional winds increase as the solar activity decreases, and the DW2 temperature amplitude increases with solar activity. The DE1 and D0 components and the DW2 winds, on the other hand, do not show a clear dependence on solar activity.

3.4. Short-Term Variability in the Upper Atmosphere

[33] Figure 16 shows the simulated meridional wind over December at 3 h intervals at 3 latitudes (46°S, the equator, and 46°N). It is clear from the plots that the temporal and spatial scales vary significantly: In the stratosphere, the variation mainly comes from episodic, quasi-stationary planetary waves; the planetary waves in the summer and equatorial MLT region show a quasiperiodicity of about 2 days. The winter MLT region is characterized by modulation of the tides, presumably due to interaction between tides and planetary waves, as well as the superposition of these waves. A semidiurnal variation is prominent between 90–130 km, and diurnal variation dominates at higher altitudes. The diurnal variation in the upper thermosphere is evidently strongly affected by solar heating, as also seen in the tidal analysis in section 3.3. It is interesting to note that, although the solar input (f10.7) is kept constant in this simulation, the amplitude of the diurnal variation changes from day to day. As shown in section 3.3 and in Figure 15, nonmigrating tides can affect the variability in the upper thermosphere. The day-to-day variability of these tides may result from tidal interaction with planetary waves in the MLT [*Hagan and Roble*, 2001; *Liu et al.*, 2007], and/or variation of the parameterized gravity wave forcing.

[34] A wavelet analysis is performed to better quantify these different scales. In Figure 17, wavelet amplitudes in the frequency domain for wavenumbers 1, 2, 3, 4 and larger than 4 are calculated for the meridional wind at 46°S in the mesopause (3.3×10^{-4} hPa) and the upper thermosphere (4×10^{-8} hPa). At the mesopause, the dominant oscillation periods are 5 day for wavenumber 1, semidiurnal with ~3 day modulation for wavenumber 2, 2.5 day for wavenumber 3, 2 day and 5 day for wavenumber 4, and 4.4 day for variations with wavenumbers larger than 4. It should be noted that the quasi-two-day wave with wavenumber 3 is usually observed in the MLT in the southern hemisphere during the "window period" of late January and February, when the atmospheric wind conditions allow the propagation and amplification of the wave [*Plumb*, 1981; *Liu et al.*, 2004]. Similar variability with tidal periods and planetary wave periods in the MLT region is also found in NOAA WAM simulations [*Fuller-Rowell et al.*, 2008]. In the upper thermosphere, the dominant period for wavenumber 1 is diurnal and its amplitude varies with time. For wavenumbers 2 and 3, there are still significant migrating tidal components (semidiurnal and terdiurnal, respectively), which are responsible for the MTM in the thermosphere. The wavelet analysis also shows that all wavenumbers in the upper thermosphere have a diurnal period.

[35] Figure 18 shows the root mean square (rms) temperature relative to the total temperature from synoptic scale perturbations (wavenumbers larger than 4). It is evident that the relative rms temperature is largest in the MLT (up to 5%), corresponding to rms temperature of 10–15 K. In the middle and upper thermosphere, the rms temperature is also ~10 K but the relative values are smaller. WACCM-X simulations also show that the rms temperature in the upper

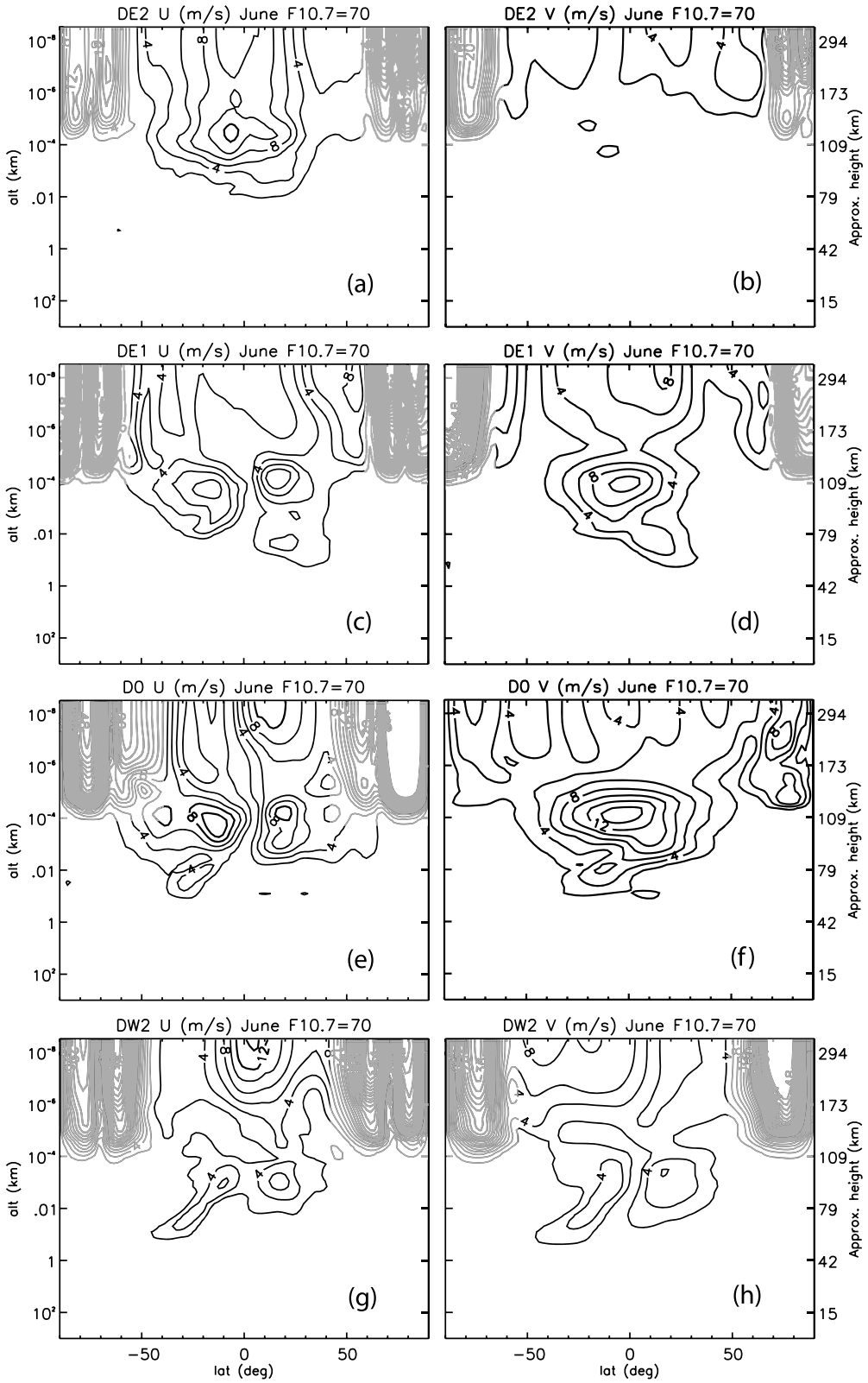

Figure 15. Nonmigrating diurnal tides of (left) zonal and (right) meridional winds for June from WACCM-X simulations under solar minimum conditions. (a and b) DE2, (c and d) DE1, (e and f) D0, (g and h): DW2. Large spectral components in aurora region are shaded. Contour intervals: 2 ms^{-1}.

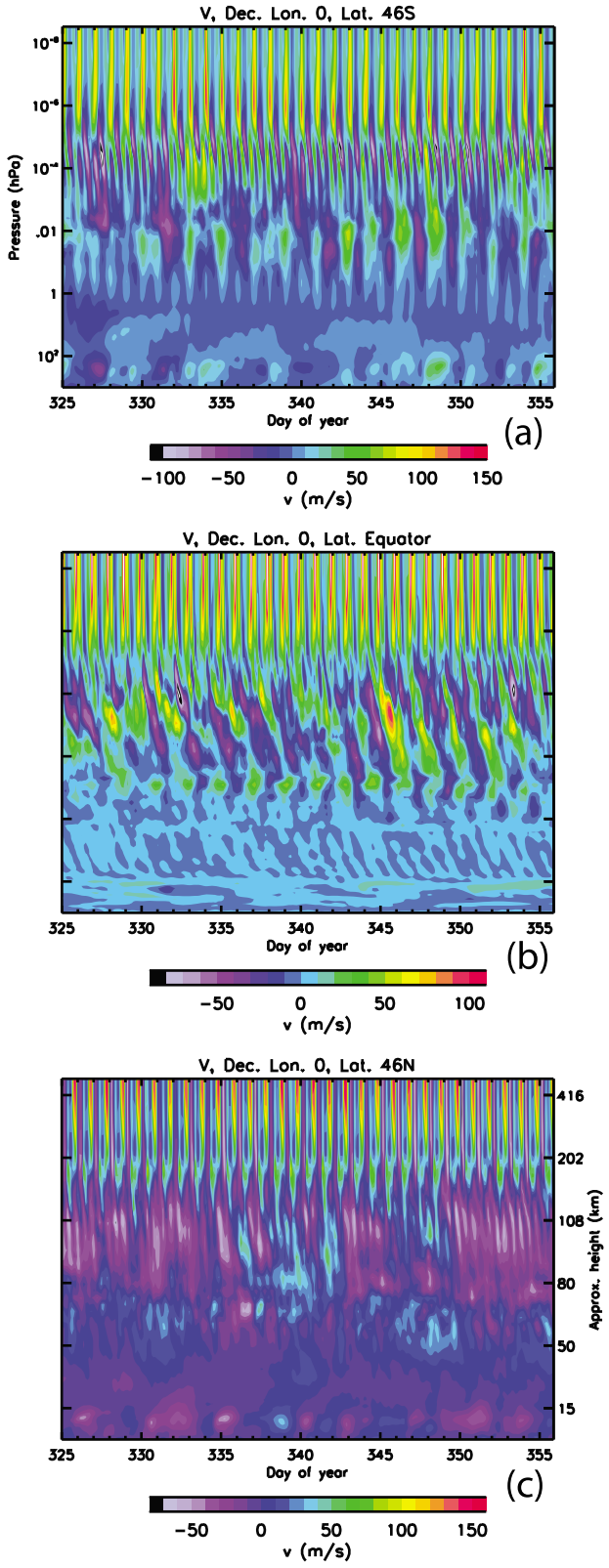

Figure 16. Neutral meridional wind from WACCM-X at (a) 46°S, (b) the equator, and (c) 46°N for December.

atmosphere is quite similar for different solar conditions. Because most planetary waves with large wavenumbers are trapped in the troposphere, the perturbations are probably caused by the tides and gravity waves resolved by the model that grow exponentially with altitude [*Liu et al.*, 2009]. Both gravity waves and tides are increasingly damped at higher altitudes in the thermosphere. As a result of the maximum synoptic variability as well as large tidal perturbations, the MLT appears to be the region with the most complex temporal and spatial scales in WACCM-X simulations. This can also be visualized through an animation of the model zonal wind (see auxiliary material Animation S1).[1] The rms could be even larger in reality, because mesoscale gravity waves are not resolved in the model. The large variability in this region can have important implications for the ionosphere through the wind dynamo, which will be studied once the ionospheric electrodynamics is implemented in WACCM-X.

4. Summary

[36] A whole atmosphere model, NCAR WACCM-X, that extends from the Earth's surface to the upper thermosphere has been developed. This model is based on the NCAR WACCM3, which is a superset of NCAR CAM3 and now the standard atmospheric component of the NCAR Climate Community System Model (CCSM). WACCM-X resolves the dynamical, physical and photochemical processes in the whole atmosphere domain. The globally averaged number densities of the major species and the most important middle and upper atmosphere species in oxygen, hydrogen, nitrogen and carbon compounds are in general agreement with those obtained from the NCAR Global Mean Model. The globally averaged number densities of 5 ion species (O^+, O_2^+, NO^+, N^+, and N_2^+) and electrons are also in reasonable agreement with those from the Global Mean Model below the F2 peak. The globally averaged $[O]/[N_2]$ ratio in the upper thermosphere shows a semiannual variation, with maximum at equinoxes and minimum at solstices, and the ratio increases with solar activity. These are in good agreement with empirical model results.

[37] The zonal mean temperature and winds from WACCM-X are consistent with our climatological understanding of these fields in the middle and upper atmosphere at solstice and equinox, reproducing several key features, including the jet reversal and reverse (summer-to-winter) latitudinal temperature gradient at the mesopause, and the superrotation at low to middle latitudes in the upper thermosphere. The temperature in the upper thermosphere is cooler (by ~200 K) than the empirical model and TIE-GCM results under solar maximum conditions. One heating source that is currently not accounted for in the model is the collisions of thermal electrons, ions and neutrals. The temperature around ~100 km, on the other hand, is warmer (by ~10–20 K) than those from observations and models at all seasons, due to excessive heating in the gravity wave parameterization scheme.

[38] The migrating diurnal tide in the mesosphere and lower thermosphere displays seasonal variation similar to the TIMED SABER and TIDI observations, with a primary

[1] Auxiliary materials are available in the HTML. doi:10.1029/2010JA015586.

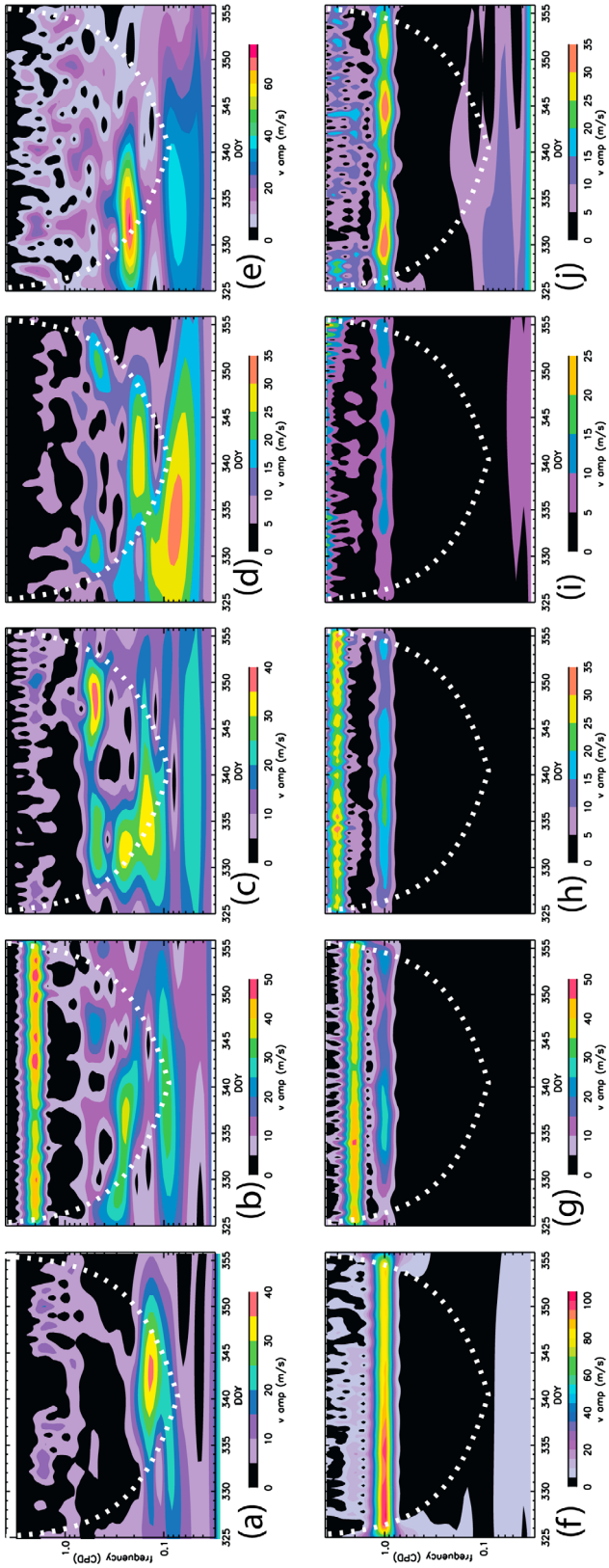

Figure 17. Wavelet analysis in frequency domain of the wavenumber amplitudes of the meridional wind at 46°S (Figure 16a). (top) Mesopause (3.3×10^{-4} hPa). (bottom) Upper thermosphere (4×10^{-8} hPa). (a and f): wavenumber 1, (b and g) wavenumber 2, (c and h) wavenumber 3, (d and i) wavenumber 4, (e and j) wavenumbers larger than 4.

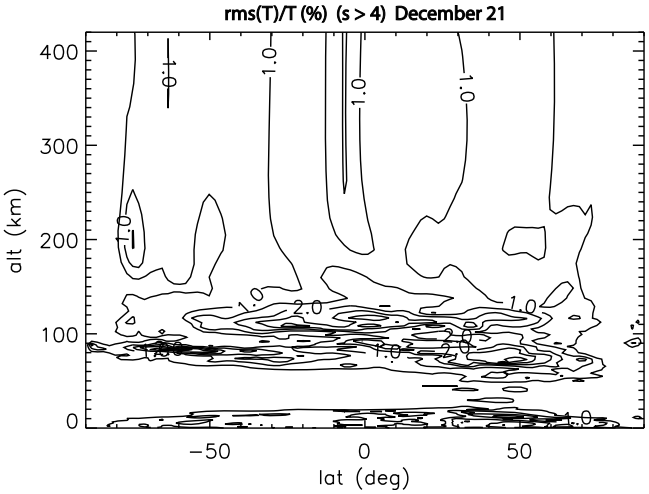

Figure 18. Relative root mean square (rms) temperature for components with wavenumbers larger than 4. Contour interval: 0.5%.

peak at March equinox and a secondary peak at September equinox, but the tidal amplitudes from the model are smaller. The tidal amplitudes in the MLT do not show a clear dependence on solar activity, while the thermospheric tides are strongly dependent on the solar activity. The nonmigrating DE3 component from the model is in good agreement with TIMED SABER and TIDI measurements. In the thermosphere, the DE3, DE2 and DW2 are in reasonable agreement with CHAMP measurements. The amplitudes of the semidiurnal migrating and nonmigrating SW1 and SW3 components from the model are generally weak compared with observations. The tidal components vary strongly from day to day, probably due to interaction with planetary waves and among tides. Model simulations demonstrate that the atmosphere between 50–200 km is highly dynamically variable with complex temporal and spatial scales, as a result of growing tidal and gravity waves, their interaction with the planetary waves, and probably also due to flow instability. The variability in this region has important implications for the mass, momentum, and energy exchange between the mesosphere and thermosphere, and for the ionospheric wind dynamo. These should be further studied using WACCM-X with self-consistent electrodynamics, which is currently under development.

[39] **Acknowledgments.** This work is in part supported by the Office of Naval Research (N00014-07-C-0209), National Science Foundation CEDAR grants ATM-0535466 and ATM-0836386, and NASA LWS Strategic Capability grant NNX09AJ83G. J.O. was supported by the DFG through its CAWSES program, grant OB 299/2-3. The National Center for Atmospheric Research is sponsored by the National Science Foundation.

[40] Robert Lysak thanks the reviewers for their assistance in evaluating this paper.

References

Akmaev, R. A., T. J. Fuller-Rowell, F. Wu, J. M. Forbes, X. Zhang, A. F. Anghel, M. D. Iredell, S. Moorthi, and H. M. Juang (2008), Tidal variability in the lower thermosphere: Comparison of Whole Atmosphere Model (WAM) simulations with observations from TIMED, *Geophys. Res. Lett.*, *35*, L03810, doi:10.1029/2007GL032584.

Andrews, D. G., J. R. Holton, and C. B. Leovy (1987), *Middle Atmosphere Dynamics*, 489 pp., Academic, Orlando, Fla.

Banks, P. M., and G. Kockarts (1973), *Aeronomy, Part B*, 355 pp., Elsevier, New York.

Beagley, S. R., J. deGrandpre, J. N. Koshyk, N. A. McFarlane, and T. G. Shepherd (1997), Radiative-dynamical climatology of the first-generation Canadian Middle Atmosphere Model, *Atmos. Ocean*, *35*, 293–331.

Becker, E., and D. C. Fritts (2006), Enhanced gravity-wave activity and interhemispheric coupling during the MaCWAVE/MIDAS northern summer program 2002, *Ann. Geophys.*, *24*, 1175–1188.

Boville, B. A. (1995), Middle atmosphere version of CCM2 (MACCM2): Annual cycle and interannual variability, *J. Geophys. Res.*, *100*, 9017–9039.

Bowman, B. R. (2004), The semiannual thermospheric density variation from 1970 to 2002 between 200–1100 km, paper 2004-114 presented at AAS/AIAA Spaceflight Mechanics Meeting, Am. Astron. Soc., Maui, Ha.

Brasseur, G. P., D. A. Hauglustaine, S. Walters, P. J. Rasch, J.-F. Muller, C. Granier, and X.-X. Tie (1998), MOZART: A global chemical transport model for ozone and related chemical tracers: 1. Model description, *J. Geophys. Res.*, *103*, 28,265–28,289.

Burrage, M. D., M. E. Hagan, W. R. Skinner, D. L. Wu, and P. B. Hays (1995a), Long-term variability in the solar diurnal tide observed by HRDI and simulated by the GSWM, *Geophys. Res. Lett.*, *22*, 2641–2644.

Burrage, M. D., D. L. Wu, W. R. Skinner, D. A. Ortland, and P. B. Hays (1995b), Latitude and seasonal dependence of the semidiurnal tide observed by the High-Resolution Doppler Imager, *J. Geophys. Res.*, *100*, 11,313–11,321.

Chang, J. L., and S. K. Avery (1997), Observations of the diurnal tide in the mesosphere and lower thermosphere over Christmas Island, *J. Geophys. Res.*, *102*, 1895–1907.

Chang, L. C., S. E. Palo, and H.-L. Liu (2009), Short-term variation of the $s = 1$ nonmigrating semidiurnal tide during the 2002 sudden stratospheric warming, *J. Geophys. Res.*, *114*, D03109, doi:10.1029/2008JD010886.

Charney, J. G., and P. G. Drazin (1961), Propagation of planetary scale disturbances from the lower to the upper atmosphere, *J. Geophys. Res.*, *66*, 83–109.

Chau, J. L., B. G. Fejer, and L. P. Goncharenko (2009), Quiet variability of equatorial $\mathbf{E} \times \mathbf{B}$ drifts during a sudden stratospheric warming event, *Geophys. Res. Lett.*, *36*, L05101, doi:10.1029/2008GL036785.

Coy, L., S. E. Siskind, S. D. Eckermann, J. P. McCormack, D. R. Allen, and T. F. Hogan (2005), Modeling the August 2002 minor warming event, *Geophys. Res. Lett.*, *32*, L07808, doi:10.1029/2005GL022400.

Dickinson, R. E., E. C. Ridley, and R. G. Roble (1981), A three-dimensional general circulation model of the thermosphere, *J. Geophys. Res.*, *86*, 1499–1512.

Dickinson, R. E., E. C. Ridley, and R. G. Roble (1984), Thermospheric general circulation with coupled dynamics and composition, *J. Atmos. Sci.*, *41*, 205–219.

Drob, D. P., et al. (2008), An empirical model of the Earth's horizontal wind fields: HWM07, *J. Geophys. Res.*, *113*, A12304, doi:10.1029/2008JA013668.

Dunkerton, T. J. (1982), Theory of the mesopause semiannual oscillation, *J. Atmos. Sci.*, *39*, 2681–2690.

Fejer, B. G., and M. C. Kelley (1980), Ionospheric irregularities, *Rev. Geophys.*, *18*, 401–454.

Fomichev, V. I., J.-P. Blanchet, and D. S. Turner (1998), Matrix parameterization of the 15μm CO_2 band cooling in the middle and upper atmosphere for variable CO_2 concentration, *J. Geophys. Res.*, *103*, 11,505–11,528.

Forbes, J. M. (1995), Tidal and planetary waves, in *The Upper Mesosphere and Lower Thermosphere: A Review of Experiment and Theory*, *Geophys. Monogr. Ser.*, vol. 87, edited by R. M. Johnson and T. L. Killeen, pp. 67–87, AGU, Washington, D. C.

Forbes, J. M., M. E. Hagan, X. Zhang, and J. Hackney (1999), Upper atmosphere tidal variability due to latent heat release in the tropical troposphere, *Adv. Space Res.*, *24*, 1515–1521.

Forbes, J. M., X. Zhang, S. Palo, J. Russell, C. J. Mertens, and M. Mlynczak (2008), Tidal variability in the ionospheric dynamo region, *J. Geophys. Res.*, *113*, A02310, doi:10.1029/2007JA012737.

Forbes, J. M., S. L. Bruinsma, X. Zhang, and J. Oberheide (2009), Surface-exosphere coupling due to thermal tides, *Geophys. Res. Lett.*, *36*, L15812, doi:10.1029/2009GL038748.

Fritts, D. C., and M. J. Alexander (2003), Gravity wave dynamics and effects in the middle atmosphere, *Rev. Geophys.*, *41*(1), 1003, doi:10.1029/2001RG000106.

Froehlich, C. (2000), Observations of irradiance variations, *Space Sci. Rev.*, *94*, 15–24.

Fujiwara, H., and Y. Miyoshi (2010), Morphological features and variations of temperature in the upper thermosphere simulated by a whole atmosphere GCM, *Ann. Geophys.*, *28*, 427–437.

Fuller-Rowell, T. J. (1995), The dynamics of the lower thermosphere, in *The Upper Mesosphere and Lower Thermosphere: A Review of Experiment and Theory*, *Geophys. Monogr. Ser.*, vol. 87, edited by R. M. Johnson and T. L. Killeen, pp. 23–36, AGU, Washington, D. C.

Fuller-Rowell, T. J. (1998), The "thermospheric spoon": A mechanism for the semiannual density variation, *J. Geophys. Res.*, *103*, 3951–3956.

Fuller-Rowell, T. J., et al. (2008), Impact of terrestrial weather on the upper atmosphere, *Geophys. Res. Lett.*, *35*, L09808, doi:10.1029/2007GL032911.

Garcia, R. R. (2009), Large-scale atmospheric waves observed by TIMED/SABER, paper presented at 17th Conference on Atmospheric and Oceanic Fluid Dynamics Joint With the 15th Conference on Middle Atmosphere, Am. Meteorol. Soc., Stowe, Vt., 8–12 June.

Garcia, R. R., T. J. Dunkerton, R. S. Lieberman, and R. A. Vincent (1997), Climatology of the semiannual oscillation of the tropical middle atmosphere, *J. Geophys. Res.*, *102*, 26,019–26,032.

Garcia, R. R., D. R. Marsh, D. E. Kinnison, B. A. Boville, and F. Sassi (2007), Simulation of secular trends in the middle atmosphere, 1950–2003, *J. Geophys. Res.*, *112*, D09301, doi:10.1029/2006JD007485.

Goncharenko, L., and S.-R. Zhang (2008), Ionospheric signatures of sudden stratospheric warming: Ion temperature at middle latitude, *Geophys. Res. Lett.*, *35*, L21103, doi:10.1029/2008GL035684.

Hagan, M. E., and R. G. Roble (2001), Modeling diurnal tidal variability with the National Center for Atmospheric Research thermosphere-ionosphere-mesosphere-electrodynamics general circulation model, *J. Geophys. Res.*, *106*, 24,869–24,882.

Hagan, M. E., J. M. Forbes, and F. Vial (1995), On modeling migrating solar tides, *Geophys. Res. Lett.*, *22*, 893–896.

Hagan, M. E., C. McLandress, and J. M. Forbes (1997), Diurnal tidal variability in the upper mesosphere and lower thermosphere, *Ann. Geophys.*, *15*, 1176–1186.

Hagan, M. E., M. D. Burrage, J. M. Forbes, J. Hackney, W. J. Randel, and X. Zhang (1999), GSWM-98: Results for migrating solar tides, *J. Geophys. Res.*, *104*, 6813–6828.

Hagan, M. E., A. Maute, and R. G. Roble (2009), Tropospheric tidal effects on the middle and upper atmosphere, *J. Geophys. Res.*, *114*, A01302, doi:10.1029/2008JA013637.

Harper, R. M. (1972), Nighttime meridional neutral winds near 350 km at low to mid-latitudes, *J. Atmos. Terr. Phys.*, *35*, 2023–2034.

Hauglustaine, D. A., G. P. Brasseur, S. Walters, P. J. Rasch, J.-F. Muller, L. K. Emmons, and M. A. Carroll (1998), MOZART: A global chemical transport model for ozone and related chemical tracers: 2. Model results and evaluation, *J. Geophys. Res.*, *103*, 28,291–28,335.

Häusler, K., H. Lühr, M. E. Hagan, A. Maute, and R. G. Roble (2010), Comparison of CHAMP and TIME-GCM nonmigrating tidal signals in the thermospheric zonal wind, *J. Geophys. Res.*, *115*, D00I08, doi:10.1029/2009JD012394.

Hays, P. B., and D.-L. Wu (1994), Observations of the diurnal tide from space, *J. Atmos. Sci.*, *51*, 3077–3093.

Heelis, R. A. (2004), Electrodynamics in the low and middle latitude ionosphere: A tutorial, *J. Atmos. Sol. Terr. Phys.*, *66*, 825–838.

Herrero, F. A., and N. W. Spencer (1982), On the horizontal distribution of the equatorial thermospheric midnight temperature maximum and its seasonal-variation, *Geophys. Res. Lett.*, *9*, 1179–1182.

Hines, C. O. (1960), Internal atmospheric gravity waves at ionospheric heights, *Can. J. Phys*, *38*, 1441–1481.

Holton, J. R., and H. Tan (1980), The influence of the equatorial quasi-biennial oscillation on the global circulation at 50 mb, *J. Atmos. Sci.*, *37*, 2200–2208.

Horowitz, L. W., et al. (2003), A global simulation of tropospheric ozone and related tracers: Description and evaluation of MOZART, version 2, *J. Geophys. Res.*, *108*(D24), 4784, doi:10.1029/2002JD002853.

Immel, T. J., E. Sagawa, S. L. England, S. B. Henderson, M. E. Hagan, S. B. Mende, H. U. Frey, C. M. Swenson, and L. J. Paxton (2006), Control of equatorial ionospheric morphology by atmospheric tides, *Geophys. Res. Lett.*, *33*, L15108, doi:10.1029/2006GL026161.

Karlsson, B., C. McLandress, and T. G. Shepherd (2009), Inter-hemispheric mesospheric coupling in a comprehensive middle atmosphere model, *J. Atmos. Sol. Terr. Phys.*, *71*, 518–530.

Kinnison, D. E., et al. (2007), Sensitivity of chemical tracers to meteorological parameters in the MOZART-3 chemical transport model, *J. Geophys. Res.*, *112*, D20302, doi:10.1029/2006JD007879.

Kockarts, G. (1980), Nitric oxide cooling in the terrestrial thermosphere, *Geophys. Res. Lett.*, *7*, 137–140.

Lieberman, R. S., J. Oberheide, M. E. Hagan, E. E. Remsberg, and L. L. Gordley (2004), Variability of diurnal tides and planetary waves during November 1978–May 1979, *J. Atmos. Sol. Terr. Phys.*, *66*, 517–528.

Lin, S.-J. (2004), A "vertically-Lagrangian" finite-volume dynamical core for global atmospheric models, *Mon. Weather Rev.*, *132*, 2293–2307.

Lindzen, R. S. (1981), Turbulence and stress owing to gravity wave and tidal breakdown, *J. Geophys. Res.*, *86*, 9707–9714.

Liu, H.-L., and R. G. Roble (2002), A study of a self-generated stratospheric sudden warming and its mesospheric/lower thermospheric impacts using coupled TIME-GCM/CCM3, *J. Geophys. Res.*, *107*(D23), 4695, doi:10.1029/2001JD001533.

Liu, H.-L., and R. G. Roble (2005), Dynamical coupling of the stratosphere and mesosphere in the 2002 Southern Hemisphere major stratospheric sudden warming, *Geophys. Res. Lett.*, *32*, L13804, doi:10.1029/2005GL022939.

Liu, H.-L., E. R. Talaat, R. G. Roble, R. S. Lieberman, D. M. Riggin, and J.-H. Yee (2004), The 6.5-day wave and its seasonal variability in the middle and upper atmosphere, *J. Geophys. Res.*, *109*, D21112, doi:10.1029/2004JD004795.

Liu, H. L., et al. (2007), Comparative study of short-term tidal variability, *J. Geophys. Res.*, *112*, D18108, doi:10.1029/2007JD008542.

Liu, H.-L., F. Sassi, and R. R. Garcia (2009), Error growth in a whole atmosphere climate model, *J. Atmos. Sci.*, *66*, 173–186.

Liu, H.-L., W. Wang, A. D. Richmond, and R. G. Roble (2010), Ionospheric variability due to planetary waves and tides for solar minimum conditions, *J. Geophys. Res.*, *115*, A00G01, doi:10.1029/2009JA015188.

Maeda, S., T. J. Fuller-Rowell, and D. S. Evans (1989), Zonally averaged dynamical and compositional response of the thermosphere to auroral activity during September 18–24, 1984, *J. Geophys. Res.*, *94*, 16,869–16,883.

Manney, G. L., M. J. Schwartz, K. Krueger, M. L. Santee, S. Pawson, J. N. Lee, W. H. Daffer, R. A. Fuller, and N. J. Livesey (2009), Aura Microwave Limb Sounder observations of dynamics and transport during the record-breaking 2009 Arctic stratospheric major warming, *Geophys. Res. Lett.*, *36*, L12815, doi:10.1029/2009GL038586.

Manzini, E., M. A. Giorgetta, M. Esch, L. Kornblueh, and E. Roeckner (2006), The influence of sea surface temperatures on the northern winter stratosphere: Ensemble simulations with the MAECHAM5 model, *J. Clim.*, *19*, 3863–3881.

Matsuno, T. (1971), A dynamical model of the stratospheric sudden warming, *J. Atmos. Sci.*, *28*, 1479–1494.

Mayr, H. G., J. G. Mengel, E. R. Talaat, H. S. Porter, and K. L. Chan (2003), Non-migrating diurnal tides generated with planetary waves in the mesosphere, *Geophys. Res. Lett.*, *30*(16), 1832, doi:10.1029/2003GL017877.

McCormack, J. P., et al. (2004), NOGAPS-ALPHA model simulations of stratospheric ozone during the SOLVE2 campaign, *Atmos. Chem. Phys.*, *4*, 2401–2423.

McLandress, C. M. (2002a), The seasonal variation of the propagating diurnal tide in the mesosphere and lower thermosphere. Part I: The role of gravity waves and planetary waves, *J. Atmos. Sci.*, *59*, 893–906.

McLandress, C. M. (2002b), The seasonal variation of the propagating diurnal tide in the mesosphere and lower thermosphere. Part II: The role of tidal heating and zonal mean winds, *J. Atmos. Sci.*, *59*, 907–922.

McLandress, C. M., G. G. Shepherd, B. H. Solheim, M. D. Burrage, P. B. Hays, and W. R. Skinner (1996), Combined mesosphere/thermosphere winds using WINDII and HRDI data from the Upper Atmosphere Research Satellite, *J. Geophys. Res.*, *101*, 10,441–10,453.

Miyoshi, Y., and H. Fujiwara (2003), Day-to-day variations of migrating diurnal tide simulated by a GCM from the ground surface to the exobase, *Geophys. Res. Lett.*, *30*(15), 1789, doi:10.1029/2003GL017695.

Miyoshi, Y., H. Fujiwara, J. M. Forbes, and S. L. Bruinsma (2009), Solar terminator wave and its relation to the atmospheric tide, *J. Geophys. Res.*, *114*, A07303, doi:10.1029/2009JA014110.

Myrabø, H. K., C. S. Deehr, and B. Lybekk (1984), Polar cap OH airglow rotational temperatures at the mesopuase during a stratospheric warming event, *Planet. Space Sci.*, *32*, 853–856.

Nakamura, T., D. C. Fritts, J. R. Isler, T. Tsuda, R. A. Vincent, and I. M. Reid (1997), Short-period fluctuations of the diurnal tide observed with low-latitude MF and meteor radars during CADRE: Evidence for gravity wave/tidal interactions, *J. Geophys. Res.*, *102*, 26,225–26,238.

Oberheide, J., and J. M. Forbes (2008), Tidal propagation of deep tropical cloud signatures into the thermosphere from timed observations, *Geophys. Res. Lett.*, *35*, L04816, doi:10.1029/2007GL032397.

Oberheide, J., and O. A. Gusev (2002), Observation of migrating and non-migrating diurnal tides in the equatorial lower thermosphere, *Geophys. Res. Lett.*, *29*(24), 2167, doi:10.1029/2002GL016213.

Oberheide, J., Q. Wu, T. L. Killeen, M. E. Hagan, and R. G. Roble (2006), Diurnal nonmigrating tides from TIMED Doppler Interferometer wind data: Monthly climatologies and seasonal variations, *J. Geophys. Res.*, *111*, A10S03, doi:10.1029/2005JA011491.

Oberheide, J., J. M. Forbes, K. Häusler, Q. Wu, and S. L. Bruinsma (2009), Tropospheric tides from 80 to 400 km: Propagation, interannual variability, and solar cycle effects, *J. Geophys. Res.*, *114*, D00I05, doi:10.1029/2009JD012388.

Paetzold, H. K., and H. Zschorner (1961), *The Structure of the Upper Atmosphere and its Variations After Satellite Observations, Space Research II*, 958 pp., North-Holland, Amsterdam.

Pancheva, D. V. (2000), Evidence for nonlinear coupling of planetary waves and tides in the lower thermosphere over Bulgaria, *J. Atmos. Sol. Terr. Phys.*, *62*, 115–132.

Pancheva, D. V., and N. J. Mitchell (2004), Planetary waves and variability of the semidiurnal tide in the mesosphere and lower thermosphere over Esrange (68°N, 21°E) during winter, *J. Geophys. Res.*, *109*, A08307, doi:10.1029/2004JA010433.

Picone, J. M., A. E. Hedin, D. P. Drob, and A. C. Aikin (2002), NRLMSISE-00 empirical model of the atmosphere: Statistical comparisons and scientific issues, *J. Geophys. Res.*, *107*(A12), 1468, doi:10.1029/2002JA009430.

Plumb, R. A. (1981), Instability of the distorted polar night vortex: A theory of stratospheric warmings, *J. Atmos. Sci.*, *38*, 2514–2531.

Qian, L. Y., R. G. Roble, S. C. Solomon, and T. J. Kane (2006), Calculated and observed climate change in the thermosphere, and a prediction for solar cycle 24, *Geophys. Res. Lett.*, *33*, L23705, doi:10.1029/2006GL027185.

Qian, L. Y., S. C. Solomon, and T. J. Kane (2009), Seasonal variation of thermospheric density and composition, *J. Geophys. Res.*, *114*, A01312, doi:10.1029/2008JA013643.

Randall, C. E., V. L. Harvey, D. E. Siskind, J. France, P. F. Bernath, C. D. Boone, and K. A. Walker (2009), NO_x descent in the Arctic middle atmosphere in early 2009, *Geophys. Res. Lett.*, *36*, L18811, doi:10.1029/2009GL039706.

Rees, M. H., and R. G. Roble (1975), Observations and theory of the formation of stable auroral red arcs, *Rev. Geophys. Space Phys.*, *13*, 201–242.

Ren, S., S. M. Polavarapu, and T. G. Shepherd (2008), Vertical propagation of information in a middle atmosphere data assimilation system by gravity-wave drag feedbacks, *Geophys. Res. Lett.*, *35*, L06804, doi:10.1029/2007GL032699.

Richmond, A. D. (1983), Thermospheric dynamics and electrodynamics, in *Solar-Terrestrial Physics*, *Astrophys. Space Sci. Lib.*, vol. 104, edited by R. L. Carovillano and J. M. Forbes, pp. 523–607, D. Reidel, Dordrecht, Netherlands.

Richmond, A. D., M. Blanc, B. A. Emery, R. H. Wand, B. G. Fejer, R. F. W. S. Ganguly, P. Amayenc, R. A. Behnke, C. Calderon, and J. V. Evans (1980), An empirical model of quiet-day ionospheric electric fields at middle and low latitudes, *J. Geophys. Res.*, *85*, 4658–4664.

Richmond, A. D., E. C. Ridley, and R. G. Roble (1992), A thermosphere/ionosphere general circulation model with coupled electrodynamics, *Geophys. Res. Lett.*, *19*, 601–604.

Richter, J. H., and R. R. Garcia (2006), On the forcing of the Mesospheric Semi-Annual Oscillation in the Whole Atmosphere Community Climate Model, *Geophys. Res. Lett.*, *33*, L01806, doi:10.1029/2005GL024378.

Roble, R. G. (1995), Energetics of the mesosphere and thermosphere, in *The Upper Mesosphere and Lower Thermosphere: A Review of Experiment and Theory*, *Geophys. Monogr. Ser.*, vol. 87, edited by R. M. Johnson and T. L. Killeen, pp. 1–21, AGU, Washington, D. C.

Roble, R. G. (2000), On the feasibility of developing a global atmospheric model extending from the ground to the exosphere, in *Atmospheric Science Across the Stratopause*, *Geophys. Monogr. Ser.*, vol. 123, edited by D. E. Siskind, S. D. Eckermann, and M. E. Summers, pp. 53–67, AGU, Washington, D. C.

Roble, R. G., and R. E. Dickinson (1989), How will changes in carbon-dioxide and methane modify the mean structure of the mesosphere and thermosphere, *Geophys. Res. Lett.*, *16*, 1441–1444.

Roble, R. G., and E. C. Ridley (1987), An auroral model for the NCAR thermosphere general circulation model (TGCM), *Ann. Geophys.*, *5A*, 369–382.

Roble, R. G., and E. C. Ridley (1994), A thermosphere-ionosphere-mesosphere-electrodynamics general circulation model (TIME-GCM): Equinox solar cycle minimum simulations (30–500 km), *Geophys. Res. Lett.*, *21*, 417–420.

Roble, R. G., R. E. Dickinson, and E. C. Ridley (1982), Global circulation and temperature structure of thermosphere with high-latitude plasma convection, *J. Geophys. Res.*, *87*, 1599–1614.

Sagawa, E., T. J. Immel, H. U. Frey, and S. B. Mende (2005), Longitudinal structure of the equatorial anomaly in the nighttime ionosphere observed by IMAGE/FUV, *J. Geophys. Res.*, *110*, A11302, doi:10.1029/2004JA010848.

Sassi, F., D. Kinnison, B. A. Boville, R. R. Garcia, and R. G. Roble (2004), Effect of El Niño–Southern Oscillation on the dynamical, thermal, and chemical structure of the middle atmosphere, *J. Geophys. Res.*, *109*, D17108, doi:10.1029/2003JD004434.

Schmidt, H., et al. (2006), The HAMMONIA chemistry climate model: Sensitivity of the mesopause region to the 11-year solar cycle and CO_2 doubling, *J. Clim.*, *19*, 3903–3931.

She, C.-Y. (2004), Initial full-diurnal-cycle mesopause region lidar observations: Diurnal-means and tidal perturbations of temperature and winds over Fort Collins, CO (41°N 105°W), *J. Atmos. Sol. Terr. Phys.*, *66*, 663–674.

She, C.-Y., et al. (2004), Tidal perturbations and variability in mesopause region over Fort Collins, CO (41N, 105W): Continuous multi-day temperature and wind lidar observations, *Geophys. Res. Lett.*, *31*, L24111, doi:10.1029/2004GL021165.

Solomon, S. C., and L. Qian (2005), Solar extreme-ultraviolet irradiance for general circulation models, *J. Geophys. Res.*, *110*, A10306, doi:10.1029/2005JA011160.

Swinbank, R., and D. A. Ortland (2003), Compilation of wind data for the Upper Atmosphere Research Satellite (UARS) Reference Atmosphere Project, *J. Geophys. Res.*, *108*(D19), 4615, doi:10.1029/2002JD003135.

Thomas, G. E. (1996), Global change in the mesosphere-lower thermosphere region: Has it already arrived?, *J. Atmos. Terr. Phys.*, *58*, 1629–1656.

Vadas, S. L., and D. C. Fritts (2001), Gravity wave radiation and mean responses to local body forces in the atmosphere, *J. Atmos. Sci.*, *58*, 2249–2279.

Vadas, S. L., and D. C. Fritts (2006), Gravity wave penetration into the thermosphere: Sensitivity to solar cycle variations and mean winds, *Ann. Geophys.*, *26*, 3841–3861.

Vadas, S. L., and H.-L. Liu (2009), Generation of large-scale gravity waves and neutral winds in the thermosphere from the dissipation of convectively generated gravity waves, *J. Geophys. Res.*, *114*, A10310, doi:10.1029/2009JA014108.

Vincent, R. A., S. Kovalam, D. C. Fritts, and J. R. Isler (1998), Long-term MF radar observations of solar tides in the low-latitude mesosphere: Interannual variability and comparisons with the GSWM, *J. Geophys. Res.*, *103*, 8667–8683.

Walker, J. C. G. (1977), *Evolution of the Atmosphere*, Macmillan, New York.

Walterscheid, R. L., G. G. Sivjee, and R. G. Roble (2000), Mesospheric and lower thermospheric manifestation of a stratospheric warming event over Eureka, Canada (80°N), *Geophys. Res. Lett.*, *27*, 2897–2900.

Ward, W. E., J. Oberheide, M. Riese, P. Preusse, and D. Offermann (1999), Tidal signatures in temperature data from CRISTA 1 mission, *J. Geophys. Res.*, *104*, 16,391–16,403.

Ward, W. E., V. I. Fomichev, and S. Beagley (2005), Nonmigrating tides in equinox temperature fields from the extended Canadian Middle Atmosphere Model (CMAM), *Geophys. Res. Lett.*, *32*, L03803, doi:10.1029/2004GL021466.

Weimer, D. R. (1995), Models of high-latitude electric potentials derived with a least error fit of spherical harmonic coefficients, *J. Geophys. Res.*, *100*, 19,595–19,608.

Woods, T., and G. Rottman (2002), Solar ultraviolet variability over time periods of aeronomic interest, in *Atmospheres in the Solar System: Comparative Aeronomy*, *Geophys. Monogr. Ser.*, vol. 130, edited by M. Mendillo, A. Nagy, and J. H. Waite, pp. 221–234, AGU, Washington, D. C.

Wu, Q., et al. (2008a), Global distribution and interannual variations of mesospheric and lower thermospheric neutral wind diurnal tide: 1. Migrating tide, *J. Geophys. Res.*, *113*, A05308, doi:10.1029/2007JA012542.

Wu, Q., et al. (2008b), Global distribution and interannual variations of mesospheric and lower thermospheric neutral wind diurnal tide: 2. Nonmigrating tide, *J. Geophys. Res.*, *113*, A05309, doi:10.1029/2007JA012543.

Xu, J., H.-L. Liu, W. Yuan, A. K. Smith, R. G. Roble, C. J. Mertens, J. M. Russell III, and M. G. Mlynczak (2007), Mesopause structure from TIMED/SABER observations, *J. Geophys. Res.*, *112*, D09102, doi:10.1029/2006JD007711.

Xu, J., A. K. Smith, H.-L. Liu, W. Yuan, Q. Wu, G. Jiang, M. G. Mlynczak, and J. M. Russell III (2009), Estimation of the equivalent Rayleigh friction in MLT region from the migrating diurnal tides observed by TIMED, *J. Geophys. Res.*, *114*, D23103, doi:10.1029/2009JD012209.

Yu, J. R., R. States, S. J. Franke, C. S. Gardner, and M. Hagan (1997), Observations of tidal temperature and wind perturbations in the mesopause region above Urbana, IL (40 degrees N, 88 degrees W), *Geophys. Res. Lett.*, *24*, 1207–1210.

Yuan, T., C.-Y. She, D. A. Krueger, F. Sassi, R. Garcia, R. G. Roble, H.-L. Liu, and H. Schmidt (2008), Climatology of mesopause region temperature, zonal wind, and meridional wind over Fort Collins, Colorado (41°N, 105°W), and comparison with model simulations, *J. Geophys. Res.*, *113*, D03105, doi:10.1029/2007JD008697.

Zhang, X. L., J. M. Forbes, M. E. Hagan, J. M. Russell, S. E. Palo, C. J. Mertens, and M. G. Mlynczak (2006), Monthly tidal temperatures 20–120 km from TIMED/SABER, *J. Geophys. Res.*, *111*, A10S08, doi:10.1029/2005JA011504.

B. T. Foster, M. E. Hagan, H.-L. Liu, J. M. McInerney, A. Maute, L. Qian, A. D. Richmond, R. G. Roble, and S. C. Solomon, High Altitude Observatory, National Center for Atmospheric Research, PO Box 3000, Boulder, CO 80307-3000, USA. (liuh@ucar.edu)

R. R. Garcia, D. Kinnison, D. R. Marsh, and A. K. Smith, Atmospheric Chemistry Division, National Center for Atmospheric Research, 3450 Mitchell Ln., Boulder, CO 80307-3000, USA.

J. Oberheide, Department of Physics and Astronomy, Clemson University, Clemson, SC 29631-0978, USA.

J. Richter, Climate and Global Dynamics, National Center for Atmospheric Research, PO Box 3000, Boulder, CO 80307-3000, USA.

F. Sassi, Space Science Division, Naval Research Laboratory, 4555 Overlook Ave. SW, Washington, DC 20375, USA.